

Interval Isogeometric Analysis for Coping with Geometric Uncertainty

Nataly A. Manque^{a,*}, Jan Liedmann^b, Franz-Joseph Barthold^c, Marcos A. Valdebenito^a,
Matthias G.R. Faes^{a,d}

^a*Chair for Reliability Engineering, TU Dortmund University, Leonhard-Euler-Str. 5, Dortmund 44227, Germany*

^b*Institute of Structural Mechanics and Dynamics in Aerospace Engineering, University of Stuttgart,
Pfaffenwaldring 27, 70569 Stuttgart, Germany*

^c*Institut für Baumechanik, Statik und Dynamik, Technische Universität Dortmund, August-Schmidt-Str. 8, 44227
Dortmund, Germany*

^d*International Joint Research Center for Engineering Reliability and Stochastic Mechanics, Tongji University,
Shanghai 200092, China*

Abstract

Geometric uncertainty poses a significant challenge in many engineering sub-disciplines ranging from structural design to manufacturing processes, often attributed to the underlying manufacturing technology and operating conditions. When combined with geometric complexity, this phenomenon can result in substantial disparities between numerical predictions and the actual behavior of mechanical systems. One of the underlying causes lies in the initial design phase, where insufficient information impedes the development of robust numerical models due to epistemic uncertainty in system dimensions. In such cases, set-based methods, like intervals, prove useful for characterizing these uncertainties by employing lower and upper bounds to define uncertain input parameters. Nevertheless, employing interval methods for treating geometric uncertainties can become computationally demanding, especially when traditional methods like finite element analysis (FEA) are utilized to represent the system. This is due to the necessity of performing iterative analyses for different realizations of geometry within the bounds of uncertain parameters, requiring the repeated execution of the meshing process and thereby escalating the numerical effort. Moreover, the process of remeshing introduces a second challenge by disrupting the continuity of the underlying optimization problem inherent in interval analysis, further complicating the computational procedure. In this work, the potential of Isogeometric Analysis (IGA) for quantifying geometric uncertainties characterized by intervals is explored. IGA utilizes the same basis functions, Non-Uniform Rational B-Splines (NURBS), employed in Computer-Aided Design (CAD) to approximate solution fields in numerical analysis. This integration enhances

31 the accurate description of complex shapes and interfaces while maintaining geometric fidelity
32 throughout the simulation process. The primary advantage of employing IGA for uncertainty
33 quantification lies in its ability to control the system's geometry through the position of control
34 points, which define the shape of NURBS. Consequently, alterations in the model's geometry can
35 be achieved by varying the position of these control points, thereby bypassing the numerical costs
36 associated with remeshing when performing uncertainty quantification considering intervals. To
37 propagate geometric uncertainties, a gradient-based optimization (GBO) algorithm is applied to
38 determine the lower and upper bounds of the system response. The corresponding sensitivities
39 are computed from the IGA model with a variational approach. Two case studies involving linear
40 systems with uncertain geometric parameters demonstrate that the proposed strategy accurately
41 estimates uncertain stress triaxiality.

42 *Keywords:* Isogeometric analysis (IGA), Geometric uncertainty, Interval analysis, Variational
43 Sensitivity Analysis, Stress Triaxiality.

44 *Highlights:*

- 45 • Proposes Isogeometric Analysis (IGA) to handle geometric uncertainties.
- 46 • Geometric uncertainties are propagated without the need for remeshing procedures.
- 47 • Incorporates variational sensitivity analysis for efficient propagation of interval uncertainties.
- 48 • Validates efficiency through stress triaxiality analysis in both 2D and 3D mechanical systems.

49 **1. Introduction**

50 Geometric uncertainties are prevalent in fields as diverse as aerospace, automotive, robotics,
51 and civil, mechanical, and biomedical engineering, where precision and robustness are paramount [1].
52 These uncertainties can pose significant challenges to ensuring the performance and safety of crit-
53 ical systems. In industrial manufacturing, for example, geometric uncertainties play a critical role
54 in the design and production process. For such reason, manufacturing geometric uncertainty will
55 be the focus of this work. Manufacturing geometric uncertainty involves discrepancies between
56 nominal models and the actual behavior of a component, potentially resulting in inaccuracies in

57 dimensions, shape, and tolerances of the manufactured part [2, 3]. This phenomenon can con-
58 tribute to diminished working efficiency, variations in the performance of mechanical systems, as
59 well as decreased service life and operational reliability [4, 5]. Various sources can contribute to
60 geometric uncertainties in manufacturing processes. For instance, wear and deflection of cutting
61 tools may lead to deviations from the intended geometry during machining processes [6]. In-
62 accuracies and imperfections in the machine tool itself, such as backlash, thermal expansion, or
63 misalignment, can also introduce geometric uncertainties [7, 8, 9]. Additionally, elastic and plastic
64 deformation of materials during machining or forming processes may induce deviations from the
65 desired geometry [10]. Moreover, inconsistent or imprecise fixtures and clamping mechanisms can
66 introduce variations in part positioning, impacting the final geometry [11]. Since all these causes
67 can affect the final operating conditions of the system, such geometric uncertainties must be taken
68 into account to accurately study the behavior of mechanical components.

69 The geometry information available during the initial design phase is typically limited and
70 inaccurate due to the aforementioned manufacturing sources of geometric uncertainty. This lack
71 of knowledge impedes the development of robust numerical models due to epistemic uncertainty
72 in system dimensions. In recent years, set-based methods have been developed to address un-
73 certainty arising from information scarcity [12, 13]. These methods have been widely applied to
74 estimate system responses resulting from epistemic uncertainty, including fuzzy analysis [14, 15],
75 imprecise probabilities [16, 17], and interval analysis [18, 19, 20, 21]. Among these techniques,
76 interval analysis has proven particularly practical when dealing with limited information [22, 23].
77 In interval analysis, a parameter affected by epistemic uncertainty is defined by lower and upper
78 bounds [24]. This approach is especially suitable at an earlier stage of design when only the range
79 of variation of the uncertain parameters is known, and the available information is insufficient to
80 determine the nature of the distribution within the interval [25]. Once uncertainty is described by
81 intervals, it is necessary to propagate this uncertainty to the response of interest (e.g., displace-
82 ments, strains, and stresses). Traditionally, interval uncertain parameters are propagated through
83 a finite element model (FE) to obtain information about the extremes of the system response using
84 a global optimization approach [26]. Nevertheless, performing interval analysis can be computa-
85 tionally expensive, especially for complex models with numerous uncertain parameters [27]. The
86 need to repeatedly evaluate the numerical model over different interval realizations increases the
87 computational cost. This cost is even higher when geometric parameters are uncertain, as in the

88 case of manufacturing uncertainties. This is because each of these evaluations requires rebuilding
89 the finite element geometry (i.e., the mesh), which is costly, time-consuming, and increases the in-
90 accuracy of the geometry representation. Moreover, a second problem with remeshing procedures
91 is that it destroys the continuity of the optimization problem underlying interval analysis.

92 The motivation for this paper is to explore the potential of Isogeometric Analysis (IGA) [28]
93 for quantifying geometric uncertainties characterized by intervals. In this technique, geometries
94 described by Non-Uniform Rational B-Splines (NURBS) based on Computer-Aided Design (CAD)
95 are used directly in the analysis framework, without performing any geometric approximation
96 as in the Finite Element Analysis (FEA) [29]. Therefore, the main principle of IGA is to use
97 NURBS basis functions to construct and manipulate the exact shape of CAD geometries and
98 as a means for their numerical analysis [30]. Notably, NURBS exhibit meaningful properties,
99 including non-negativity, unit partitioning, local support, and smoothness, ensuring high-order
100 continuity between elements [31]. As a result, one of the main advantages of IGA is its geometric
101 accuracy [32], no matter how coarse the discretization may be [28]. Since IGA allows users to
102 easily handle complex geometries, this technique seems suitable for uncertainty quantification
103 (UQ) [31]. To the best of our knowledge, a few applications of IGA for UQ have been developed.
104 The work of [33] uses the Stochastic Isogeometric Analysis (SIGA) to study the free vibration of
105 functionally graded plates with spatially varying random material properties. In their work, the
106 elastic modulus and mass density were considered uncertain properties, which were modeled as
107 homogeneous Gaussian random fields. Spectral stochastic isogeometric analysis (SSIGA) [34] for
108 stochastic linear elasticity problems considering spatially dependent uncertain Young's modulus
109 has also been investigated. The contribution of [35] proposes an IGA-based framework for solving
110 the uncertainty problem of composite shells. The work of [36] presents a framework for uncertainty
111 quantification and robust shape optimization of acoustic structures. The approach is based on
112 the Boundary Element Method (BEM) and the Polynomial Chaos Expansion (PCE), where an
113 IGA BEM is used to calculate shape sensitivities. Another contribution of SIGA to the analysis
114 of shape uncertainty has been proposed by [37], where the authors combine IGA and PCE to
115 address uncertainty described by random fields. Nevertheless, the application of IGA to quantify
116 geometric uncertainties under limited data has not been explored. Hence, it is the object of this
117 work to examine its coupling with interval analysis. When using IGA to model a system, the
118 geometry can be controlled by the position of the control points that define the shape of the

119 NURBS [38]. This is an advantage for quantifying geometric uncertainty. This is because the
120 control points define the control mesh, which represents the physical structure of the system.
121 As a result, it is possible to modify the model geometry and obtain the updated field solutions
122 without going through the remeshing process [39, 40]. Therefore, by manipulating the geometry
123 through changes in the position of the control points, it is possible to avoid the numerical cost of
124 performing interval analysis using classical finite element analysis with remeshing.

125 For the propagation of geometric uncertainties, applying a gradient-based optimization (GBO)
126 algorithm [41] is proposed to determine both the lower and upper bounds of the system response.
127 The gradient of the objective function is calculated concerning each geometric uncertain param-
128 eter, from the sensitivities of the IGA model. Exploiting the key benefit of IGA to manipulate
129 the geometry, a variational formulation that allows the simultaneous computation of structural
130 response and sensitivities is applied [42]. A parameterization of the NURBS control point ma-
131 trix is applied to guide FE users in the use of IGA for uncertainty quantification. The proposed
132 strategy is tested for estimating uncertain stress triaxiality in a linear 2D hook system with un-
133 certain radius and thickness, and in a linear 3D horseshoe shape with four uncertain geometric
134 parameters.

135 The rest of the paper is organized as follows. The governing equations for the class of systems
136 considered in this work are presented in Section 2. The definition of the response of interest as
137 well as the influence of geometric uncertainty on the associated stress triaxiality response is also
138 explained. Section 3 presents the approach used to describe the uncertain parameters associated
139 with the geometry using interval analysis. The disadvantages of interval analysis for uncertainty
140 propagation in the context of FEA are discussed in detail. Section 4 provides the basics of IGA
141 analysis and the formulation of the sensitivity analysis. The applied uncertainty propagation
142 scheme is presented in Section 5, using the GBO algorithm. The implementation of the proposed
143 technique is illustrated and discussed in Section 6. Conclusions are drawn in Section 7.

144 **2. Formulation of the problem**

145 *2.1. Governing equations*

146 Consider a linear system under the influence of static loads. It is considered that the parameters
147 that characterize the geometry of the system (e.g., lengths, thicknesses, curvatures) cannot be
148 accurately determined due to problems such as lack of knowledge, vagueness, and imprecision of

149 data resulting from manufacturing processes. Consequently, the geometric input parameters are
 150 affected by epistemic uncertainty. These parameters are collected in a vector \mathbf{x} of dimension n_x .
 151 Typically, a set of partial differential equations (PDEs) must be solved to perform a structural
 152 design calculation for this system. The approximate solution of these PDEs is usually provided
 153 by a numerical model $\mathcal{M}(\mathbf{x})$. This numerical model $\mathcal{M}(\mathbf{x})$ can be constructed using the Finite
 154 Element Method (FEM) [43], Finite Difference Method (FDM) [44], Boundary Element Method
 155 (BEM) [45], or Isogeometric Analysis (IGA) [28], among others. Note that the model $\mathcal{M}(\mathbf{x})$
 156 depends on the geometric uncertain parameters \mathbf{x} . In addition, through the application of these
 157 methods, the model yields a response \mathbf{y} , which is defined as,

$$\mathcal{M}(\mathbf{x}) : \mathbf{y} = m(\mathbf{x}) \quad (1)$$

158 where m is a response function operator that maps the geometric uncertain input parameters
 159 \mathbf{x} to the output response \mathbf{y} . This response can encompass various quantities of interest, such as
 160 displacements, stresses, or strain fields. Note that the behavior of the system, given by its response
 161 \mathbf{y} , is influenced by uncertain geometric variables \mathbf{x} during the mapping with m . As a result, the
 162 response of the system is subject to uncertainties as well. The response of interest considered in
 163 this paper is discussed in Section 2.2.

164 Notably, the construction of the numerical model $\mathcal{M}(\mathbf{x})$ using the traditional finite element
 165 method can involve significant computational effort, especially when the uncertainty relates to ge-
 166 ometry. Firstly, a large number of degrees-of-freedom are typically required to discretely represent
 167 a system with traditional FEA, to accurately capture its real behavior. This becomes especially
 168 challenging when dealing with complex geometries. Secondly, the discretization step involves
 169 defining a finite element mesh that approximates the system's real geometry. To capture uncer-
 170 tainties in the geometry, this mesh needs redefinition whenever the geometry changes. As a result,
 171 the numerical model $\mathcal{M}(\mathbf{x})$ must be constructed at a high level of detail to accurately capture the
 172 complex geometry of the system and is further dependent on the mesh definition. Consequently,
 173 obtaining a solution for Eq. (1) may not be straightforward in the presence of geometric uncer-
 174 tainty. Therefore, exploring alternative methods becomes essential to reduce computational costs
 175 and increase efficiency when analyzing systems with complex geometries and uncertain parame-
 176 ters. Hence, this paper investigates Isogeometric Analysis (IGA) as an alternative method due to
 177 its advantages in handling geometry. The basis of this technique will be discussed in Section 4.

178 *2.2. Stress triaxiality*

179 As mentioned above, it is of interest to investigate a response related to the system defined
 180 in Eq. (1), e.g. for design purposes. In mechanical analysis and especially in manufacturing
 181 design, users are interested in studying damage states [46], as well as initiation of fracture pro-
 182 cesses [47]. For this purpose, analyzing the stresses resulting from the numerical simulation $\mathcal{M}(\mathbf{x})$
 183 is crucial. In particular, stress triaxiality is one of the most important factors in controlling such
 184 problems [48]. The stress triaxiality index provides useful insight into material performance under
 185 complex loading conditions. This helps in the design and optimization of structural components
 186 to improve performance and service life. By definition, stress triaxiality $\sigma_{\text{ST}}(\mathbf{x})$ is the ratio of
 187 the hydrostatic stress $\sigma_{\text{M}}(\mathbf{x})$ to a deformation-related deviatoric stress contribution $\sigma_{\text{V}}(\mathbf{x})$. In
 188 mathematical terms,

$$\sigma_{\text{ST}}(\mathbf{x}) = \frac{\sigma_{\text{M}}(\mathbf{x})}{\sigma_{\text{V}}(\mathbf{x})} \quad (2)$$

189 where, for general plane stress conditions, the hydrostatic stress corresponds to,

$$\sigma_{\text{M}}(\mathbf{x}) = \frac{\sigma_{11}(\mathbf{x}) + \sigma_{22}(\mathbf{x})}{2} \quad (3)$$

190 where σ_{11} and σ_{22} are the principal stresses, and the deviatoric stress contribution can be consid-
 191 ered as the equivalent von Mises stress,

$$\sigma_{\text{V}}(\mathbf{x}) = \sqrt{\sigma_{11}^2(\mathbf{x}) + \sigma_{22}^2(\mathbf{x}) - \sigma_{11}(\mathbf{x})\sigma_{22}(\mathbf{x}) + 3\sigma_{12}^2(\mathbf{x})} \quad (4)$$

192 where $\sigma_{12}(\mathbf{x})$ is the shear stress.

193 If the analysis is performed in a 3D system, then the hydrostatic stress is equivalent to the
 194 following

$$\sigma_{\text{M}}(\mathbf{x}) = \frac{1}{3}\text{tr}(\boldsymbol{\sigma}(\mathbf{x})), \quad (5)$$

195 where $\boldsymbol{\sigma}$ is the Cauchy stress tensor.

196 In the same way, the equivalent von Mises stress corresponds to,

$$\sigma_V(\mathbf{x}) = \left(\frac{1}{2} \left((\sigma_{11}(\mathbf{x}) - \sigma_{22}(\mathbf{x}))^2 + (\sigma_{22}(\mathbf{x}) - \sigma_{33}(\mathbf{x}))^2 + (\sigma_{33}(\mathbf{x}) - \sigma_{11}(\mathbf{x}))^2 \right) + 3(\sigma_{12}^2(\mathbf{x}) + \sigma_{23}^2(\mathbf{x}) + \sigma_{31}^2(\mathbf{x})) \right)^{\frac{1}{2}}, \quad (6)$$

197 where σ_{33} is the principal stress, and σ_{23} and σ_{31} are the shear stresses.

198 Note that since it is assumed that the geometric properties of the system are affected by
 199 epistemic uncertainty, the stress triaxiality $\sigma_{ST}(\mathbf{x})$ also depends on these geometric uncertainties,
 200 which are collected in the vector \mathbf{x} . Moreover, this uncertainty is also reflected in the von Mises
 201 $\sigma_V(\mathbf{x})$ and hydrostatic $\sigma_M(\mathbf{x})$ stresses. For example, consider a plate whose thickness varies along
 202 its domain. This variation can cause differences in hydrostatic stress at different locations, re-
 203 sulting in different magnitudes of stress triaxiality along the plate domain. In addition, if the
 204 plate has holes, inaccuracies in the shape, curvature, and location of the holes can cause stress
 205 concentration effects that change the stress state in the vicinity of the holes, thus varying the
 206 stress triaxiality.

207 Once the response of the system ($\sigma_{ST}(\mathbf{x})$ for this work) and the n_x geometric uncertain param-
 208 eters are identified, the next step is to characterize the uncertainty in those parameters. There
 209 are several techniques to characterize the uncertainty that affects stress triaxiality. One way is to
 210 resort to interval analysis following a set-based method. The next section discusses the essential
 211 definitions for incorporating this uncertainty using interval analysis.

212 **3. Interval analysis**

213 *3.1. Interval theory*

214 At an early design stage, the available data concerning the location of holes, thicknesses of
 215 elements, lengths, and shapes can be highly affected by epistemic uncertainty. In these cases,
 216 the source of uncertainty is due to a lack of knowledge produced by, for example, manufacturing
 217 processes, as was discussed in the previous sections. Typically, this data is not sufficient to build a
 218 robust numerical model to predict the behavior of mechanical components. One way to represent
 219 this type of uncertainty is to resort to interval analysis [24]. This technique has been extensively
 220 studied in finite element analysis to characterize the uncertainty in system input parameters (e.g.,
 221 material properties and loading conditions) [49]. An interval or interval scalar is a convex subset

222 of the domain of real numbers \mathbb{R} . An interval-valued parameter x^I is defined by,

$$x^I = [\underline{x}, \bar{x}] = \{x \in \mathbb{R} \mid \underline{x} \leq x \leq \bar{x}\} \quad (7)$$

223 where \underline{x} represents the lower bound and \bar{x} corresponds to the upper bound of x^I . Therefore, x^I
 224 contains all possible values that an uncertain input parameter can take, with no assumption made
 225 regarding the likelihood of those values [19]. For a better description of an interval quantity, the
 226 center or midpoint μ_{x^I} and the interval radius Δx^I are usually defined. The center of the interval
 227 is defined as,

$$\mu_{x^I} = \frac{\underline{x} + \bar{x}}{2} \quad (8)$$

228 and the interval radius corresponds to,

$$\Delta x^I = \frac{\bar{x} - \underline{x}}{2} \quad (9)$$

229 In most cases, there is more than one uncertain parameter. In this situation, the definition of
 230 an interval vector is useful. An interval vector \mathbf{x}^I is a vector in which each element is an interval,

$$\mathbf{x}^I = \left\{ \begin{array}{c} x_1^I \\ x_2^I \\ \vdots \\ x_a^I \end{array} \right\} = \{ \mathbf{x} \in \mathbb{R}^a \mid x_i \in x_i^I \} \quad (10)$$

231 with $\mathbf{x}^I \in \mathbb{IR}^a$, the domain of closed real-valued interval vectors of size a . Similarly, interval
 232 matrices are defined in $\mathbb{IR}^{a \times b}$ following the expression,

$$\mathbf{X}^I = \left\{ \begin{array}{cccc} x_{11}^I & x_{12}^I & \cdots & x_{1b}^I \\ x_{21}^I & x_{22}^I & \cdots & x_{2b}^I \\ \vdots & \vdots & \ddots & \vdots \\ x_{a1}^I & x_{a2}^I & \cdots & x_{ab}^I \end{array} \right\} = \{ \mathbf{X} \in \mathbb{R}^{a \times b} \mid x_{ij} \in x_{ij}^I \} \quad (11)$$

233 In Eq. (10) and (11), all indices in interval vectors and matrices are assumed to be independent.
 234 Consequently, an a -dimensional interval vector describes a hypercube in a -dimensional space. The
 235 lower and upper bounds of the interval scalar entries in the interval vector \mathbf{x}^I determine the vertices

236 of this hypercube [49, 26].

237 3.2. Interval analysis

238 The basic idea of interval analysis is to search, from a hypercube \mathbf{x}^I representing the uncer-
239 tain input parameters, for those parameter realizations that yield the extreme response of the
240 system [26]. If the n_x uncertain geometric parameters \mathbf{x} of Eq. (1) are characterized through
241 intervals (that is, \mathbf{x}^I), then the response of the system \mathbf{y} will be approximated by the smallest
242 hypercube \mathbf{y}^I . Typically \mathbf{y}^I is calculated following a global optimization approach. In the case
243 that the response of interest is scalar y^I , e.g. stress triaxiality (see Eq. (2)), the optimization
244 problem corresponds to,

$$\underline{y} = \min_{\mathbf{x} \in \mathbf{x}^I} m(\mathbf{x}) \quad (12)$$

$$\bar{y} = \max_{\mathbf{x} \in \mathbf{x}^I} m(\mathbf{x}) \quad (13)$$

246 where $y^I = [\underline{y}, \bar{y}]$ is the interval response of the system which is defined by its lower \underline{y} and upper
247 \bar{y} bounds. In the context of the global optimization approach (see e.g., [50], [51]), repeated de-
248 terministic analyses are required to find the lower and upper bounds of the response, exploring
249 various realizations of the uncertain geometric input parameters. Undoubtedly, the numerical
250 cost associated with finding both bounds of the response is directly influenced by the nature of
251 $m(\mathbf{x})$ and, hence, the response. If the response of the deterministic system varies monotonically
252 concerning the uncertain parameters, the Vertex Method [52], ensures an exact result for opti-
253 mizing the interval problem defined in Eq. (12) and (13). On the contrary, if the behavior of m
254 is non-monotonic, the accuracy of this approach quickly breaks down due to the limited number
255 of sample points considered to find y^I [26]. For the cases where m is non-monotonic, the opti-
256 mization procedure can be performed using black-box optimization routines [53, 54] or surrogate
257 models [55, 56]. Note that the use of surrogate models helps to reduce the cost of finding \underline{y} and
258 \bar{y} . Nevertheless, the main challenge in this context is to build an accurate approximate response
259 model, which can be quite difficult to achieve when the uncertainty is in the geometry.

260 The method used to construct $\mathcal{M}(\mathbf{x})$ also has a strong influence on the numerical cost of
261 finding the response of interest (solution of Eq. (12) and (13)). Especially when using the finite
262 element method and considering that the uncertainty is in the geometry, it would be necessary
263 to modify the discrete representation of the system (i.e. the mesh) for each of the realizations
264 required to find the bounds of the response during the optimization stage. This disadvantage is

265 caused by decoupling the meshing procedure and the numerical calculation of the field responses.
 266 One way to deal with this difficulty is to use a method that allows one to handle both geometry
 267 and solution fields simultaneously. The following section presents Isogeometric Analysis as a viable
 268 alternative for propagating geometric uncertainty.

269 4. Isogeometric analysis model

270 4.1. Structural response

271 The Isogeometric Analysis (IGA) was first proposed by Hughes et al., [28], as a means to
 272 parametrize the geometry associated with solid bodies analyzed using Finite Element Analysis
 273 (FEA). Both methods share basic ideas, however, in contrast to FEA, in IGA the geometry
 274 of the analyzed structure is not approximated by polynomial shape functions (e.g. Lagrangian
 275 basis functions) but described by a smooth geometry description used in Computer-Aided De-
 276 sign (CAD). Mostly, these descriptions are based on Non-Uniform Rational B-splines (NURBS).
 277 NURBS curves, surfaces, and volumes can be defined by knot vectors Ξ and control points. The
 278 knot vectors must have $n + p + 1$ increasing entries called knots ξ_i of the form

$$\Xi = \{\xi_1, \xi_2, \dots, \xi_{n+p+1}\}, \quad (14)$$

279 and define the parametric space as well as the NURBS order p . It also defines the C^{p-1-k} continuity
 280 conditions at the knots, where k denotes the number of repetitions of a specific knot in the knot
 281 vector Ξ . Further, n is the total number of NURBS basis functions that are defined by,

$$R_{i,p}(\xi) = \frac{w_i N_{i,p}(\xi)}{W(\xi)}, \quad 1 \leq i \leq p+1, \quad \text{with} \quad W(\xi) = \sum_{i=1}^{n_{\text{cp}}} w_i N_{i,p}(\xi), \quad (15)$$

282 where n_{cp} is the total number of NURBS control points, $w_i > 0$ are weight factors and $N_{i,p}$ are
 283 B-spline basis functions of order p defined by the Cox-de Boor recursive formulas, cf. e.g. [30, 39].
 284 NURBS curves $\mathbf{C}(\xi)$ and surfaces $\mathbf{S}(\xi, \eta)$ are respectively described by,

$$\mathbf{C}(\xi) = \sum_{i=1}^n R_{i,p}(\xi) \mathbf{P}_i, \quad \mathbf{S}(\xi, \eta) = \sum_{i=1}^n \sum_{j=1}^m R_{i,p}(\xi) R_{j,q}(\eta) \mathbf{P}_{i,j}, \quad (16)$$

285 where \mathbf{P} stores the control point coordinates, and m and q correspond to the number of NURBS
 286 basis functions, and the NURBS order in the second space dimension, respectively. Note that

287 η represents a second parametric dimension (i.e. knots in the direction of the second space
 288 dimension), which is collected in the knot vector \mathbf{H} . This knot vector \mathbf{H} can be defined following
 289 Eq. (14). Note also that this description can be extended to define volumes, which requires the
 290 addition of a third parametric coordinate.

291 In this work, problems of linear elasticity are tackled, as introduced in Section 2. Similar to
 292 standard FEA formulations, the starting point to define the field responses is the Weak Form of
 293 Equilibrium

$$R(\mathbf{u}, \mathbf{v}) = \int_{\Omega} \boldsymbol{\varepsilon}(\mathbf{u}) : \mathbb{C} : \boldsymbol{\varepsilon}(\mathbf{v}) dV - \int_{\Omega} \mathbf{b} \cdot \mathbf{v} dV - \int_{\partial\Omega} \mathbf{t} \cdot \mathbf{v} dA, \quad (17)$$

294 where $R(\mathbf{u}, \mathbf{v})$ represents the residual form of the equilibrium equation, $\boldsymbol{\varepsilon}$ denotes the linear strain
 295 tensor, and \mathbb{C} is the fourth order linear elasticity tensor. \mathbf{u} and \mathbf{v} are the displacement field and
 296 test function vectors (also known as virtual displacement field), and \mathbf{b} and \mathbf{t} are the body and
 297 traction force vectors, respectively. The physical space domain Ω is discretized using sub-domains
 298 called elements or knot-spans Ω_e that are defined in the parametric space $\tilde{\Omega}$ by the structure of
 299 the knot vectors (i.e., Ξ and \mathbf{H} in two-dimensional cases).

300 Element approximations of geometry \mathbf{X}^h , displacements \mathbf{u}^h and test functions \mathbf{v}^h read,

$$\mathbf{X}^h = \sum_{i=1}^{n_{\text{cp}}^e} R_i(\xi, \eta) \mathbf{P}_i = \mathbf{N} \mathbf{P}_e, \quad \mathbf{u}^h = \sum_{i=1}^{n_{\text{cp}}^e} R_i(\xi, \eta) \mathbf{u}_i = \mathbf{N} \mathbf{u}_e, \quad \mathbf{v}^h = \sum_{i=1}^{n_{\text{cp}}^e} R_i(\xi, \eta) \mathbf{v}_i = \mathbf{N} \mathbf{v}_e, \quad (18)$$

301 where $R_i(\xi, \eta) \equiv R_{i,p}(\xi) R_{j,q}(\eta)$, \mathbf{N} is the matrix of shape functions, and n_{cp}^e is the number of
 302 control points of an element Ω_e . \mathbf{P}_e , \mathbf{u}_e , and \mathbf{v}_e are the control point matrix, displacements, and
 303 test functions, per element, respectively.

304 Using this matrix notation, the symmetric linear strains can be approximated by,

$$\boldsymbol{\varepsilon}(\mathbf{u}^h) = \sum_{i=1}^{n_{\text{cp}}^e} \mathbf{B}_i \mathbf{u}_i = \mathbf{B} \mathbf{u}_e \quad \text{and} \quad \boldsymbol{\varepsilon}(\mathbf{v}^h) = \sum_{i=1}^{n_{\text{cp}}^e} \mathbf{B}_i \mathbf{v}_i = \mathbf{B} \mathbf{v}_e, \quad (19)$$

305 with the strain-displacement matrix \mathbf{B} and the matrix of shape functions \mathbf{N} given by,

$$\mathbf{B} = \begin{bmatrix} R_{1,x} & 0 & \dots & R_{n_{\text{cp}}^e,x} & 0 \\ 0 & R_{1,y} & \dots & 0 & R_{n_{\text{cp}}^e,y} \\ R_{1,y} & R_{1,x} & \dots & R_{n_{\text{cp}}^e,x} & R_{n_{\text{cp}}^e,y} \end{bmatrix} \quad \text{and} \quad \mathbf{N} = \begin{bmatrix} R_1 & 0 & \dots & R_{n_{\text{cp}}^e} & 0 \\ 0 & R_1 & \dots & 0 & R_{n_{\text{cp}}^e} \end{bmatrix}. \quad (20)$$

306 It is important to highlight that the discretized matrix form of the weak equilibrium equation (see
 307 Eq. (17)) only differs from the FEA formulation by the choice of the shape functions, viz.

$$R_e = \mathbf{v}_e^T \mathbf{R}_e = \mathbf{v}_e^T \left[\int_{\Omega_e} \mathbf{B}^T \mathbf{C} \mathbf{B} dV \mathbf{u}_e - \int_{\Omega_e} \mathbf{N}^T \mathbf{b} dV - \int_{\partial\Omega_e} \mathbf{N}^T \mathbf{t} dA \right] = \mathbf{v}_e^T [\mathbf{K}_e \mathbf{u}_e - \mathbf{f}_e], \quad (21)$$

308 where R_e is the residual of the elemental equilibrium equation, \mathbf{R}_e represents the elemental internal
 309 force vector, and \mathbf{C} is the constitutive matrix, which characterizes the material properties.

310 Assembling all elements and identifying the first integral of Eq. (21) as the element stiffness
 311 matrix \mathbf{K}_e , and the other two as element force vector \mathbf{f}_e , and excluding the trivial solution $\mathbf{v} = \mathbf{0}$,
 312 the discrete system of equations for solving the solution of the displacements reads,

$$\bigcup_{e=1}^{n_{el}} [\mathbf{K}_e \mathbf{u}_e - \mathbf{f}_e] = \mathbf{K} \mathbf{u} - \mathbf{F} = \mathbf{0}, \quad (22)$$

313 where $\bigcup_{e=1}^{n_{el}}$ represents a union operation over all n_{el} elements in the discretized domain, \mathbf{K} is the
 314 stiffness matrix of the system, \mathbf{F} is the force vector, and \mathbf{u} the displacement. It is noteworthy
 315 that, unlike FEA, in IGA the response in displacements is given in the positions of the control
 316 points. With the solution of Eq. (22) any response function of interest can be computed within a
 317 post-processing step similar to FEA [29]. In this study, the so-called stress triaxiality is focused,
 318 cf. Eq. (2). To provide a clearer understanding of how the system's response is obtained at
 319 control points, Figure 1 illustrates the key domains involved in integration in the IGA process,
 320 emphasizing the transition from the physical domain to the parametric and parent domains (red
 321 arrows in the figure). Figure 1 first shows the physical domain in light blue, which represents
 322 the actual geometry of the system under study. For real-world problems, this domain is often
 323 complex and may include curved shapes, as shown in the figure. Within this domain, an element
 324 Ω_e is highlighted in orange to indicate the current region where the analysis is being performed.
 325 Note that given the definition of the control points and knot vectors, four elements are used
 326 to represent the system. Also, note that the control points are not necessarily part of physical
 327 space. Moreover, observe that the control points are connected by the control mesh. The physical
 328 domain is then mapped onto the parametric domain (see element $\tilde{\Omega}_e$). Unlike traditional FEA
 329 where the physical space is directly discretized, IGA relies on this intermediate parametric space.
 330 The parametric domain is structured in a grid format defined by knot-related coordinates. The
 331 dimensions and continuity of this space are determined by the associated knot vectors and the

332 order p of the NURBS, as shown in Eqs. (14) and (15). This parametric domain plays a critical
 333 role in the IGA process because it allows for the accurate representation of elements within the
 334 physical domain using NURBS-based shape functions. Finally, the elements within the parametric
 335 domain are further mapped to the parent domain, a standardized space commonly used in FEA.
 336 The solution of the PDE is ultimately obtained at the knots within the parametric domain and
 337 then mapped back into physical space. For this mapping, it is necessary to construct a mesh in
 338 physical space for visualization purposes. Furthermore, using post-processing techniques, like in
 339 FEA, it is possible to obtain the desired response of interest [30]. A detailed explanation of the
 340 mappings used to integrate in Isogeometric Analysis can be found in [28]. It is important to note
 341 that while mesh refinement techniques exist within the IGA framework, they are beyond the scope
 342 of this study and are not explored in this work.

343 Since the objective of this work is to apply a gradient-based optimization scheme to propagate
 344 efficiently the geometric uncertainties during the interval analysis, the next subsection discusses
 345 the procedure to obtain the sensitivities of the response.

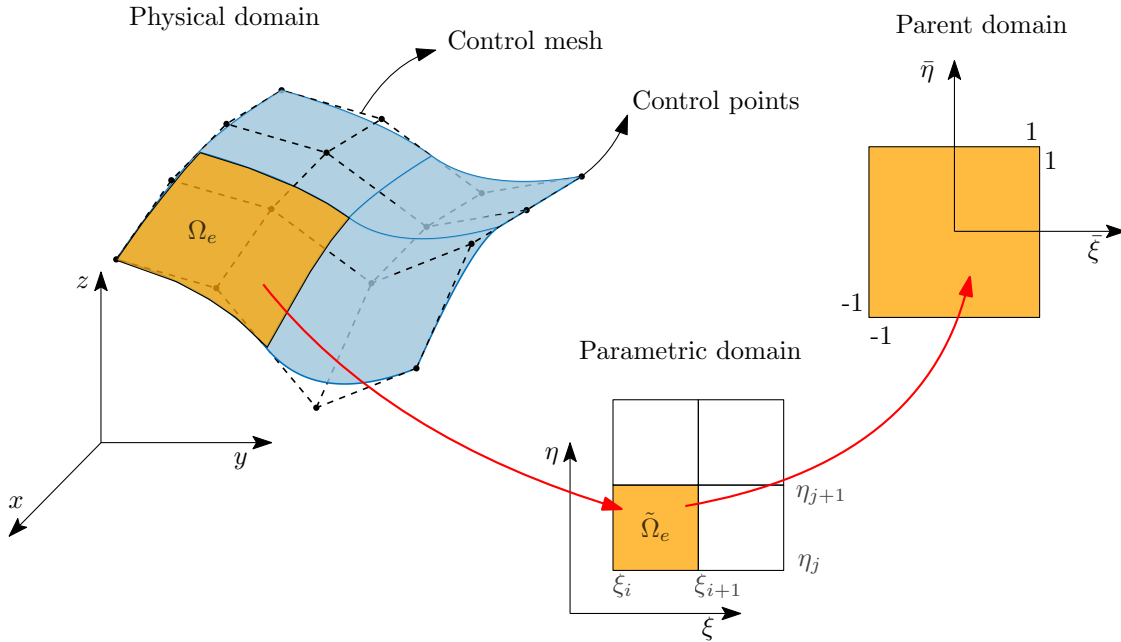


Figure 1: Domains used for integration in Isogeometric Analysis.

346 4.2. Geometric sensitivity analysis

347 Design sensitivity analysis helps to quantify the change of any response function $f(\mathbf{u}(\mathbf{x}), \mathbf{x})$,
 348 e.g. stress or strain measures, concerning alterations in chosen design (uncertain) parameters \mathbf{x} .
 349 In the following, the sensitivity relations are derived for the depicted linear elastic model, with

350 respect to the model geometry \mathbf{X} . By employing variational sensitivity analysis, as discussed in
 351 e.g. [57, 42], this change can be expressed as

$$\delta f = \delta_u f + \delta_X f = \left[\frac{\partial f}{\partial \mathbf{u}} \right] \delta \mathbf{u} + \left[\frac{\partial f}{\partial \mathbf{X}} \right] \delta \mathbf{X}. \quad (23)$$

352 Following the direct differentiation method (DDM), Eq. (22) has to hold for any design variation
 353 $\delta \mathbf{X}$, i.e. forcing a design change to satisfy the weak equilibrium condition resulting in its vanishing
 354 total variation

$$\delta R(\mathbf{u}, \mathbf{v}, \delta \mathbf{u}, \delta \mathbf{X}) = \delta_u R(\mathbf{u}, \mathbf{v}, \delta \mathbf{u}) + \delta_X R(\mathbf{u}, \mathbf{v}, \delta \mathbf{X}) = 0. \quad (24)$$

355 Using the same discretization concepts as described above, both variations in Eq. (24) can be
 356 approximated by

$$\delta_u R(\mathbf{u}, \mathbf{v}, \delta \mathbf{u}) \approx \delta_u R(\mathbf{u}^h, \mathbf{v}^h, \delta \mathbf{u}^h) = \mathbf{v}^\top \mathbf{K} \delta \mathbf{u} \quad (25)$$

357 and

$$\delta_X R(\mathbf{u}, \mathbf{v}, \delta \mathbf{X}) \approx \delta_X R(\mathbf{u}^h, \mathbf{v}^h, \delta \mathbf{X}^h) = \mathbf{v}^\top \mathbf{Q} \delta \mathbf{P}. \quad (26)$$

358 Here, \mathbf{K} denotes the global stiffness matrix, cf. Eq. (22), \mathbf{P} is the control points matrix, and \mathbf{Q}
 359 is the global pseudo-load matrix that can be derived to

$$\mathbf{Q} = \bigcup_{e=1}^{n_{el}} \mathbf{Q}_e = \bigcup_{e=1}^{n_{el}} \int_{\Omega_e} \sum_i \sum_j [\sigma(\mathbf{L}_i \mathbf{L}_j^\top - \mathbf{L}_j \mathbf{L}_i^\top) - \mathbf{B}_i^\top \mathbf{C} \mathbf{B}_j \mathbf{H}] \, dV, \quad (27)$$

360 where \mathbf{Q}_e corresponds to the element pseudo-load matrix and \mathbf{H} represents the approximation of
 361 the element displacement gradient. Further, \mathbf{L}_i is the column matrix of shape function derivatives
 362 for the i -th control point, viz.

$$\mathbf{H} = \nabla \mathbf{u}_e = \sum_i^{n_{cp}^e} \mathbf{u}_i \mathbf{L}_i^\top \quad \text{and} \quad \mathbf{L}_i = \begin{bmatrix} R_{i,x} & R_{i,y} \end{bmatrix}^\top. \quad (28)$$

363 Here, n_{cp}^e denotes the number of control points of the element e . For a detailed derivation of
 364 Eqs. (23) – (28), the interested reader is referred to e.g. [58]. Again, excluding the trivial solution
 365 $\mathbf{v} = \mathbf{0}$, the total response sensitivity matrix \mathbf{S} can be identified by rearranging the discrete total
 366 variation of the weak equilibrium condition

$$\mathbf{K} \delta \mathbf{u} = -\mathbf{Q} \delta \mathbf{P} \Rightarrow \delta \mathbf{u} = -\mathbf{K}^{-1} \mathbf{Q} \delta \mathbf{P} = \mathbf{S} \delta \mathbf{P}. \quad (29)$$

367 With the above-described variational method, the discrete sensitivity relation of the stress
 368 triaxiality can be expressed by

$$\delta\sigma_{\text{ST}} = \left[\frac{\partial\sigma_{\text{ST}}}{\partial\sigma_{\text{M}}} \frac{\partial\sigma_{\text{M}}}{\partial\boldsymbol{\sigma}} + \frac{\partial\sigma_{\text{ST}}}{\partial\sigma_{\text{V}}} \frac{\partial\sigma_{\text{V}}}{\partial\boldsymbol{\sigma}} \right] \delta\boldsymbol{\sigma}. \quad (30)$$

369 Here, the computation of the partial derivatives is straightforward. According to Eq. (23) together
 370 with Eq. (29), the total variation of the stress tensor reads

$$\delta\boldsymbol{\sigma} = \left[\frac{\partial\boldsymbol{\sigma}}{\partial\mathbf{u}} \mathbf{S} + \frac{\partial\boldsymbol{\sigma}}{\partial\mathbf{P}} \right] \delta\mathbf{P}. \quad (31)$$

371 It should be noted that not all control point coordinates are necessarily selected as design
 372 variables. In specific cases, it may be advantageous to identify a parameterization that allows for
 373 the definition of sensitivity relations e.g. regarding some geometric parameters such as lengths
 374 and radii. In these cases, a projection of the above-derived sensitivity equations utilizing a design-
 375 velocity matrix \mathbf{D} of the form

$$\delta\mathbf{P} = \mathbf{D} \delta\mathbf{x} \quad (32)$$

376 is useful, where \mathbf{x} denote the aforementioned uncertain geometric parameters of interest. With
 377 this definition in Eq. (32), the projection of Eq. (31) reads

$$\delta\boldsymbol{\sigma} = \left[\frac{\partial\boldsymbol{\sigma}}{\partial\mathbf{u}} \mathbf{S} + \frac{\partial\boldsymbol{\sigma}}{\partial\mathbf{P}} \right] \mathbf{D} \delta\mathbf{x}. \quad (33)$$

378 Observe how now the total variation of the stress tensor takes into account the derivatives with
 379 respect to the uncertain parameters. The described isogeometric model has been implemented in
 380 `MatLab` utilizing the NURBS toolbox, cf. [59] and the formulations mostly follow those described
 381 in [30].

382 5. Proposed strategy for uncertainty propagation

383 5.1. General remarks

384 The previous section defined Isogeometric Analysis (IGA) as a powerful tool for determining
 385 field responses in a numerical model using the same basis functions that define the geometry. Addi-
 386 tionally, it described how to compute the sensitivities of these field responses concerning uncertain
 387 parameters through a variational formulation. To use IGA for propagating geometric uncertainties

388 characterized as interval variables, it is crucial to strategically define the locations of control points
389 based on geometric parameters such as radius, thickness, length, etc. This approach is effective
390 because, in IGA with variational formulation, the system response and sensitivities are obtained
391 simultaneously at the control points. Nevertheless, the control points are not necessarily located
392 within the actual geometry of the system (as shown in Figure 1). Therefore, when calculating the
393 response and sensitivities, it is necessary to map them from being functions of the control points
394 (see Eq. (31)) to being functions of the uncertain geometric parameters (see Eq. (33)). Note that
395 this assumes that the response and its sensitivities have already been calculated at the location of
396 the control points, as explained in Section 4. For a comprehensive description of this procedure,
397 the reader is referred to [29] and [30]. Once the sensitivities with respect to the control points
398 are mapped to depend on the uncertain parameters, this information can be used to perform the
399 optimization for the interval analysis, i.e., to find the lower (Eq. (12)) and upper (Eq. (13)) bounds
400 of the response. This procedure is described in the next subsection.

401 *5.2. Gradient-based optimization*

402 Section 3.2 explained that interval analysis attempts to find the bounds of the response of
403 interest, given the characterization of uncertain geometric parameters as intervals. One way to
404 find these bounds is to use a gradient-based algorithm. Gradient-based optimization (GBO) is a
405 widely used method for finding the minimum or maximum of a function by iteratively descending
406 based on the direction of the gradient [41]. In this work, since information on the sensitivity of the
407 response concerning uncertain parameters is available, this method seems appropriate for interval
408 analysis. The GBO scheme used in this paper corresponds to the trust-region algorithm [60].
409 The trust-region algorithm in `MatLab` approximates the objective function with a simpler model
410 within a neighborhood called the trust region. It often uses Sequential Quadratic Programming
411 (SQP) techniques to solve the trust-region subproblem, which involves minimizing a quadratic
412 model subject to a constraint within the trust region. The gradient information is crucial in
413 this process, as it helps in the construction of the quadratic model and guides the direction of the
414 search. The algorithm ensures robust convergence, especially for nonlinear optimization problems,
415 by iteratively updating the size of the confidence region based on the accuracy of the model [61].

416 *5.3. Summary of the proposed strategy*

417 The following steps, which are also shown in Figure 2, summarize the proposed methodol-
418 ogy for performing an Isogeometric Analysis considering that the uncertainty in the geometry is

419 represented by intervals.

- 420 1. Define the numerical model (Eq. (1) and (22)) and the response of interest (Eq. (2)).
- 421 2. Identify the uncertain geometric parameters \boldsymbol{x} of the model.
- 422 3. Define the uncertainty in the geometric parameters using intervals \boldsymbol{x}^I (Eq. (7)).
- 423 4. Set the control point matrix \mathbf{P} according to the desired geometry, in terms of the uncertain
424 geometric parameters \boldsymbol{x} .
- 425 5. Compute the sensitivities of the control points matrix concerning the uncertain geometric
426 parameters, i.e. compute the design-velocity matrix \mathbf{D} .
- 427 6. Set up the NURBS associated with the model: curves, surfaces, and volumes (Eq. (16)).
- 428 7. Apply gradient-based optimization to define the lower \underline{y} and upper \bar{y} bounds of the response.
 - 429 (a) Perform Isogeometric Analysis (IGA) to calculate the response of interest (Eqs. (1
430 and (22))) and its sensitivities (Eq. (33)) using a variational analysis, i.e., compute the
431 response and sensitivities at the control points.
 - 432 (b) Post-process IGA response and obtain sensitivities depending on geometric uncertain
433 parameters \boldsymbol{x} using the sensitivities calculated in 5.

434 Note that the sequence of steps 5 and 6 is not mandatory and can be performed in any order.
435 The sensitivities calculated in Step 5 depend on the parametric definition of the control point
436 matrix \mathbf{P} and are unaffected by the subsequent NURBS model setup in Step 6. However, the
437 existing order is maintained for logical clarity and to facilitate the gradient-based optimization
438 process in Step 7.

439 6. Illustrative examples

440 6.1. 2D Linear Hook

441 The proposed methodology is applied to estimate the maximum stress triaxiality of a linear
442 two-dimensional steel hook system. The base end of the hook is fixed and a load of 20 kN is applied
443 to the top end. The material properties of the hook system are assumed deterministic and equal
444 to $E = 2 \times 10^5 \text{ N/mm}^2$ for Young's modulus and $\nu = 0.3$ for Poisson's ratio. The plane stress
445 conditions are assumed. Regarding the geometry of the system, it is assumed that the value of the
446 radius and thickness are uncertain due to the lack of knowledge at the early design stage. These
447 geometric quantities are characterized by the intervals $r^I = [10, 50] \text{ mm}$ and $t^I = [15, 40] \text{ mm}$, for

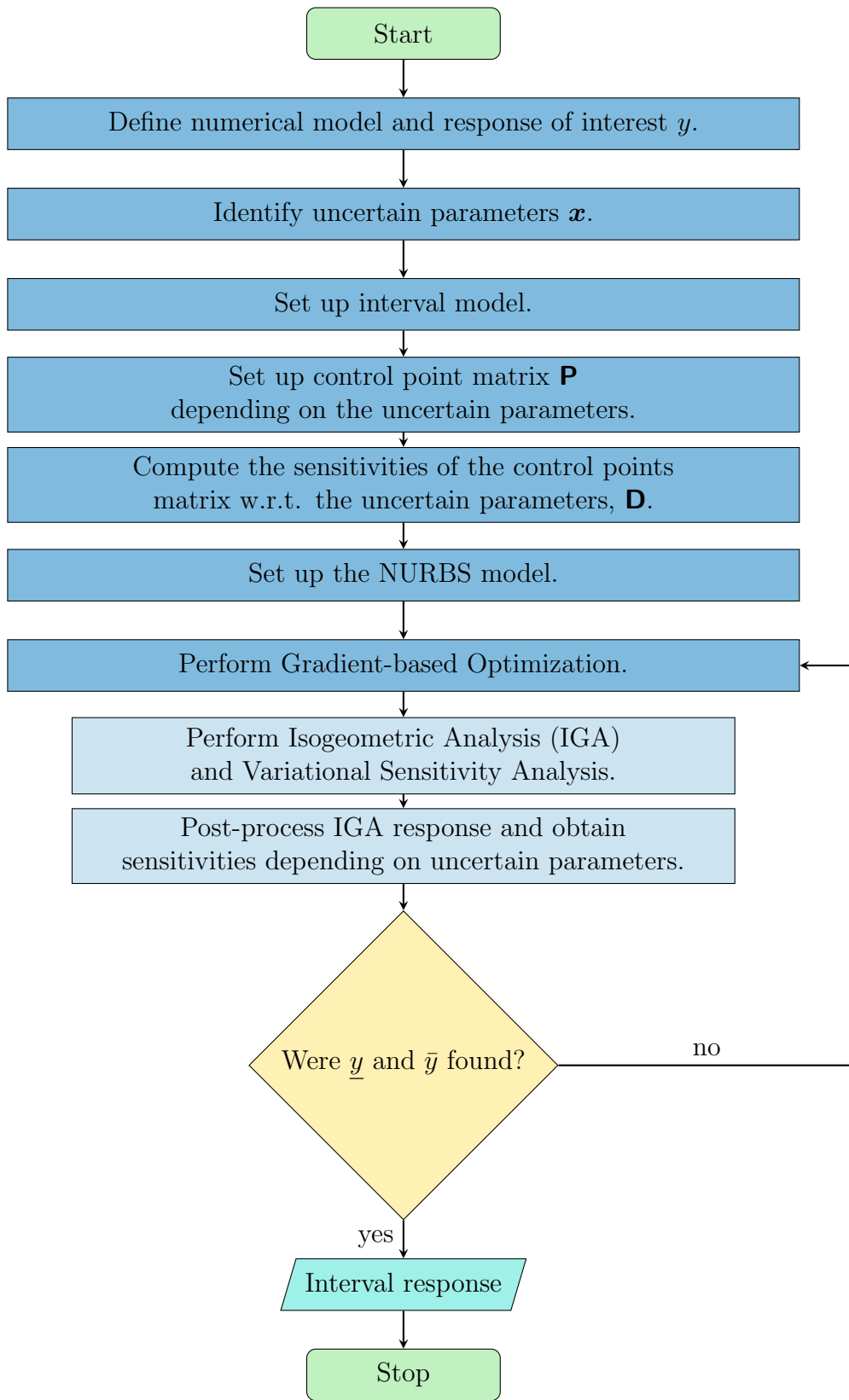


Figure 2: Flowchart of Isogeometric Analysis for quantifying geometric uncertainties characterized by intervals.

448 the radius and thickness, respectively. Note that these wide ranges are defined to emphasize the
 449 high degree of uncertainty that can exist at this design stage. Figure 3 shows the IGA model for
 450 the stress triaxiality analysis. Note that in this figure, the geometry representation is schematized
 451 considering the midpoints of the intervals, that is, $\mu_{r,I} = 30$ mm and $\mu_{t,I} = 27.50$ mm.

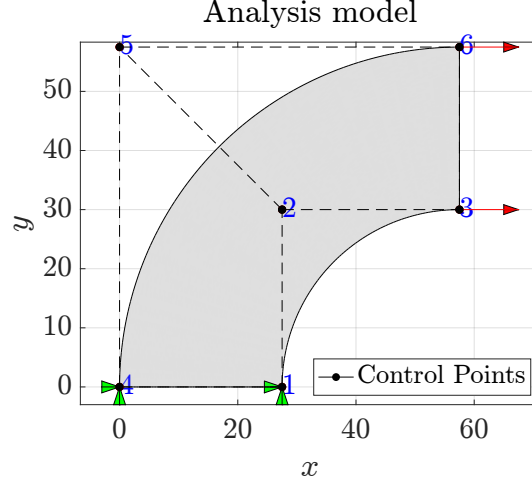


Figure 3: Hook 2D model for stress triaxiality analysis. The geometry considered corresponds to that described by the midpoints of the intervals associated with radius and thickness.

452 The NURBS surface used to represent the hook system is constructed based on $n_{cp} = 6$ control
 453 points (see Figure 3). To translate the uncertainty in the geometric input parameters to NURBS
 454 control point's matrix \mathbf{P} , a parametric representation of the coordinates of each control point in
 455 terms of r and t is proposed

$$\mathbf{P} = \begin{bmatrix} t & 0 \\ t & r \\ t+r & r \\ 0 & 0 \\ 0 & t+r \\ t+r & t+r \end{bmatrix}. \quad (34)$$

456 It is important to note that to compute sensitivities using the variational approach of sec-
 457 tion 4.2, the partial derivatives of the control point matrix \mathbf{P} with respect to r and t must also
 458 be computed, as shown in Eq. (34) and explained in Section 4.2. This is necessary to map the
 459 sensitivities from the control points to the uncertain parameters. For this task, the corresponding
 460 design-velocity matrix \mathbf{D} must be computed. By collecting all elements of the matrix \mathbf{P} in a column
 461 vector, where the coordinates of each control point are written sequentially, the design-velocity

462 matrix is equal to

$$\mathbf{D} = \begin{bmatrix} 0 & 0 & 0 & 1 & 1 & 1 & 0 & 0 & 0 & 1 & 1 & 1 \\ 1 & 0 & 1 & 0 & 1 & 0 & 0 & 0 & 0 & 1 & 1 & 1 \end{bmatrix}^T. \quad (35)$$

463 Note that each column of the design-velocity matrix \mathbf{D} contains the derivatives of all coordi-
 464 nates of the control points with respect to each geometric uncertain parameter considered. For
 465 the definition of the NURBS surface, quadratic elements with overlapping (elements can share
 466 control points or knots) are considered. The polynomial degree p of the splines associated with
 467 the knot vector in the x -direction is two, while in the y -direction is one. On the other hand, the
 468 multiplicity of the knots k is one and zero for the x -direction and the y -direction, respectively.
 469 For both directions, the weights $w = [1, \frac{1}{\sqrt{2}}, 1]$ are associated with the control points of the inner
 470 and outer curves that allow to represent the hook geometry.

471 Since this study aims to determine the variation of the maximum stress triaxiality σ_{5T} in the
 472 hook system, a gradient-based optimization approach is used to determine its lower and upper
 473 bounds. The initial point for the optimization scheme was considered as $x_0 = [\mu_{rI}, \mu_{tI}]$. The
 474 results were compared by considering the Vertex Method (VM) [52], Particle Swarm Optimization
 475 (PSO) [62], Surrogate Optimization (SO) using the Radial Basis Function (RBF) interpolation
 476 algorithm available in `Matlab` [63], and Pattern Search Optimization (PS) [64]. Table 1 shows the
 477 results for the lower bound of the maximum stress triaxiality of the hook system. Note that all
 478 evaluated methods identify the lower bound of the maximum response $\max(\sigma_{5T}) = 0.4420$ for a
 479 radius equal to $r = 10$ mm and a thickness of $t = 40$ mm. However, the Gradient-based Optimiza-
 480 tion (GBO) method appears to be the most efficient, after the Vertex Method (VM), requiring
 481 only five deterministic analyses of the hook system to identify this lower bound, highlighting the
 482 numerical advantage of the proposed strategy. It should be noted that although the VM leads
 483 to the exact results in this example (for the lower bound of the maximum stress triaxiality), this
 484 method is only accurate for cases where the response behaves monotonically over the search space.
 485 Therefore, it is recommended to use it as a reference, but one should be aware that it may under-
 486 estimate the bounds of the response. It is also important to note that the numerical cost of VM
 487 increases as a function of the number of uncertain parameters.

488 In the hook example, only two uncertain parameters are considered. This allows the behavior
 489 of the maximum stress triaxiality within the search space to be visualized. As shown in Figure 4.a,
 490 the maximum stress triaxiality is plotted as a function of the geometric parameters under consid-

Method	r in mm	t in mm	$\max(\sigma_{ST})$	No. Analysis
Vertex Method (VM)	10	40	0.4420	4
Particle Swarm Optimization (PSO)	10	40	0.4420	2254
Surrogate Optimization (SO)	10	40	0.4420	200
Pattern Search Optimization (PS)	10	40	0.4420	62
Gradient-based Optimization (GBO)	10	40	0.4420	5

Table 1: Results of optimization - lower bound of maximum stress triaxiality - Hook 2D.

491 eration. Simultaneously, Figure 4.b shows the iterations performed for the GBO approach. The
492 first observation to be made is that the response does not exhibit monotonic behavior concerning
493 both radius and thickness. Consequently, it is expected that the VM may produce inaccurate
494 results when finding the upper bound of the response, whereas the accurate result of VM for
495 the lower bound can only be explained by the fact that the lower bound is located in a corner
496 of the search space. The second observation concerns the availability of information about the
497 sensitivity of the response. This information facilitates the rapid convergence of the algorithm to
498 the optimal value. This is an indication of the efficiency and effectiveness of the GBO approach
499 in this context.

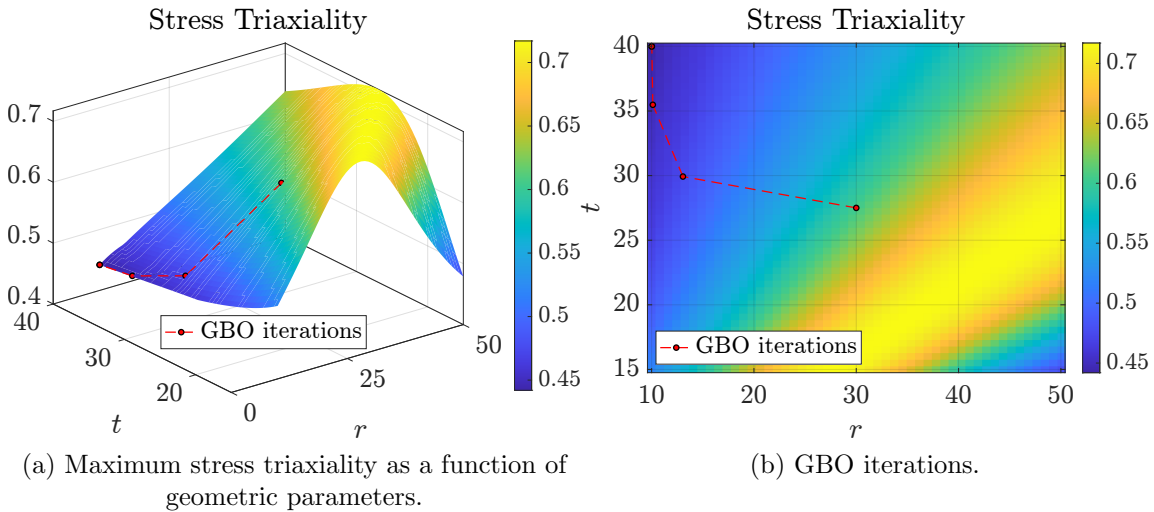


Figure 4: Distribution of the maximum stress triaxiality over the search space and iterations performed for the GBO algorithm to find the lower bound. r and t in mm.

500 The resulting geometry for the hook system with the optimum values of radius and thickness
501 for the lower bound of the response is shown in Figure 5.a. As expected, the lower limit of
502 maximum stress triaxiality is associated with a thicker hook geometry. Figure 5.b shows the

503 deformed shape due to the force applied at the right end of the hook, while Figure 5.c and 5.d
 504 show the stress triaxiality distribution over the original and deformed hook shapes, respectively.
 505 Note that the maximum values of stress triaxiality are located in the outer curve of the hook.
 506 These areas of higher stress triaxiality (closer to 0.4) are likely to be more susceptible to failure
 507 under load because they indicate a high concentration of stress.

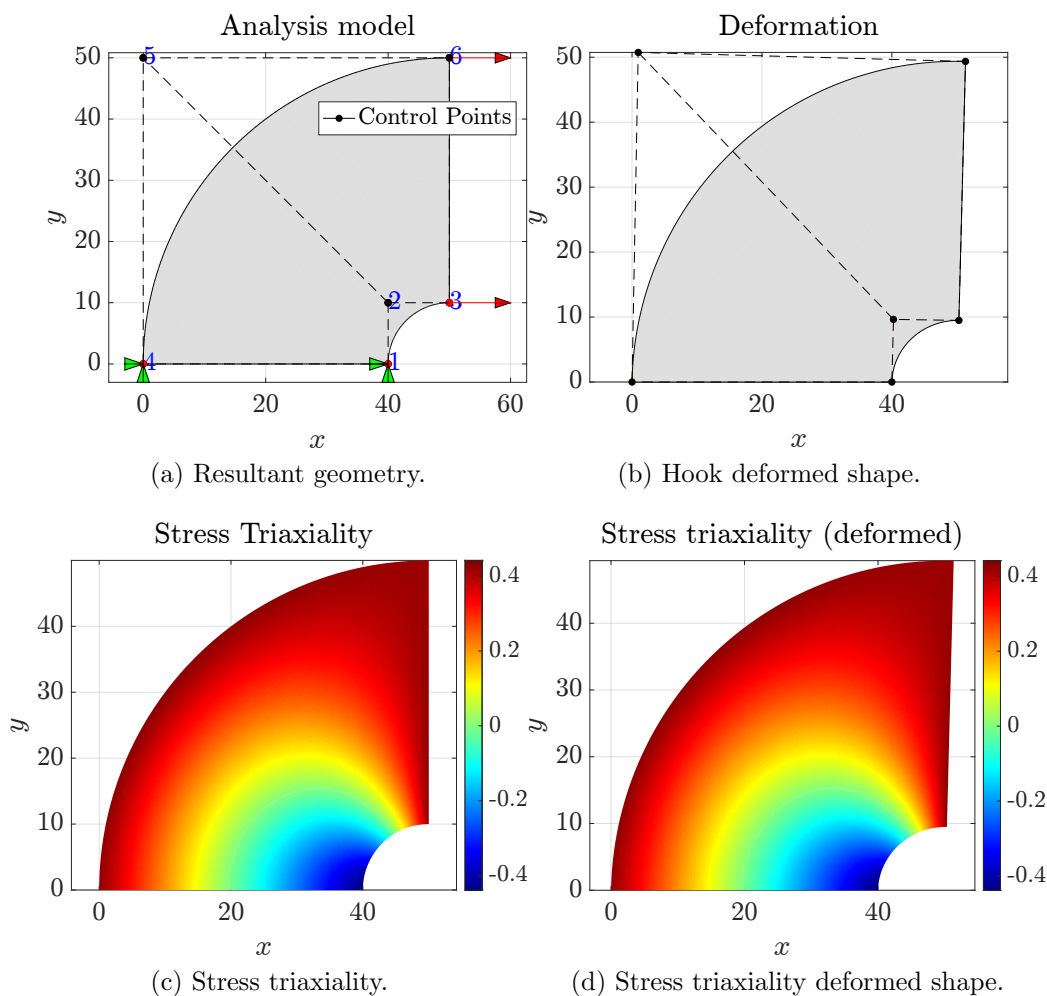


Figure 5: Resultant geometry and stress triaxiality for the lower bound results. Dimensions in mm.

508 Table 2 shows the results of the optimization procedure for the upper bound of the maximum
 509 stress triaxiality. For this bound, it is clear that the Vertex Method underestimates the optimum,
 510 which can be observed in Figure 6 due to the non-monotonicity of the maximum stress triaxiality
 511 response. Note that all optimization methods used to find the upper bound of $\max(\sigma_{ST})$, obtain the
 512 same optimal value of maximum stress triaxiality by different radius and thickness combinations.
 513 This is due to the flat behavior of stress triaxiality over the search space observed in Figure 6. In

514 the same way, as for the lower bound of the response, the GBO method appears to be the most
 515 efficient, requiring only eight deterministic analyses of the system.

Method	r in mm	t in mm	$\max(\sigma_{ST})$	No. Analysis
Vertex Method (VM)	50	40	0.6380	4
Particle Swarm Optimization (PSO)	49.6141	26.7778	0.7170	3803
Surrogate Optimization (SO)	47.4384	25.6038	0.7170	200
Pattern Search Optimization (PS)	49.0995	26.5000	0.7170	149
Gradient-based Optimization (GBO)	36.0834	19.4750	0.7170	8

Table 2: Results of optimization - upper bound of maximum stress triaxiality - Hook 2D.

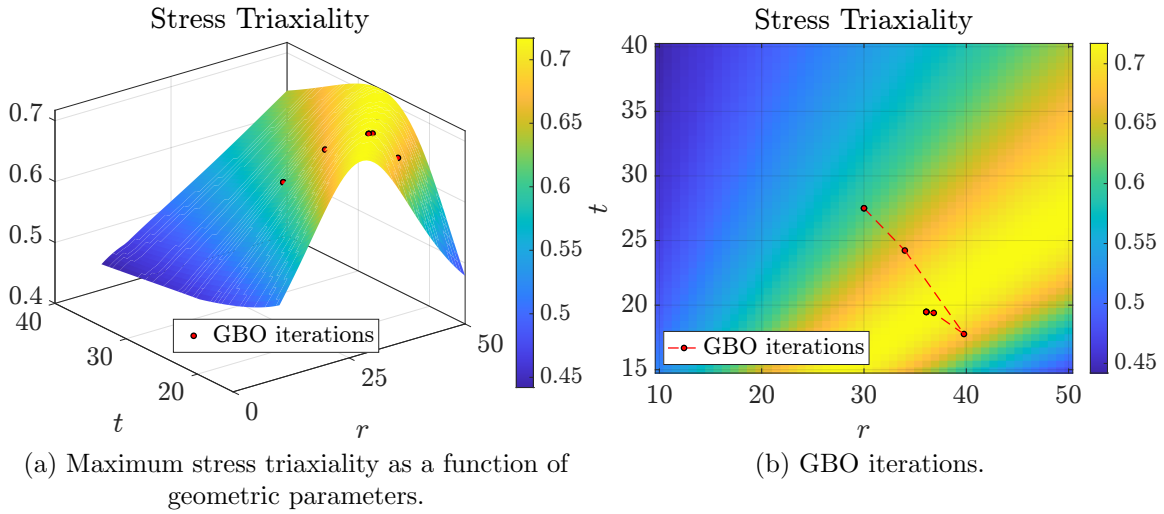


Figure 6: Distribution of the maximum stress triaxiality over the search space and iterations performed for the GBO algorithm to find the upper bound. r and t in mm.

516 Figure 7.a shows the resulting geometry for the hook system with the optimum values of radius
 517 and thickness for the upper bound of the response. A thinner hook geometry is associated with
 518 the upper bound of the maximum stress triaxiality. Figure 7.b shows the deformed geometry
 519 resulting from the force applied to the right end of the hook, while Figures 7.c and 7.d show the
 520 stress triaxiality distribution over the original and deformed hook geometry, respectively. Note
 521 that, as observed for the lower bound results, the maximum values of stress triaxiality are located
 522 in the outer curve of the hook. Again, these areas of higher stress triaxiality (closer to 0.7) are
 523 likely to be more susceptible to failure under load. Unlike the resulting geometry for the lower
 524 boundary, a wider range of stress triaxiality values is now observed in the hook shape.

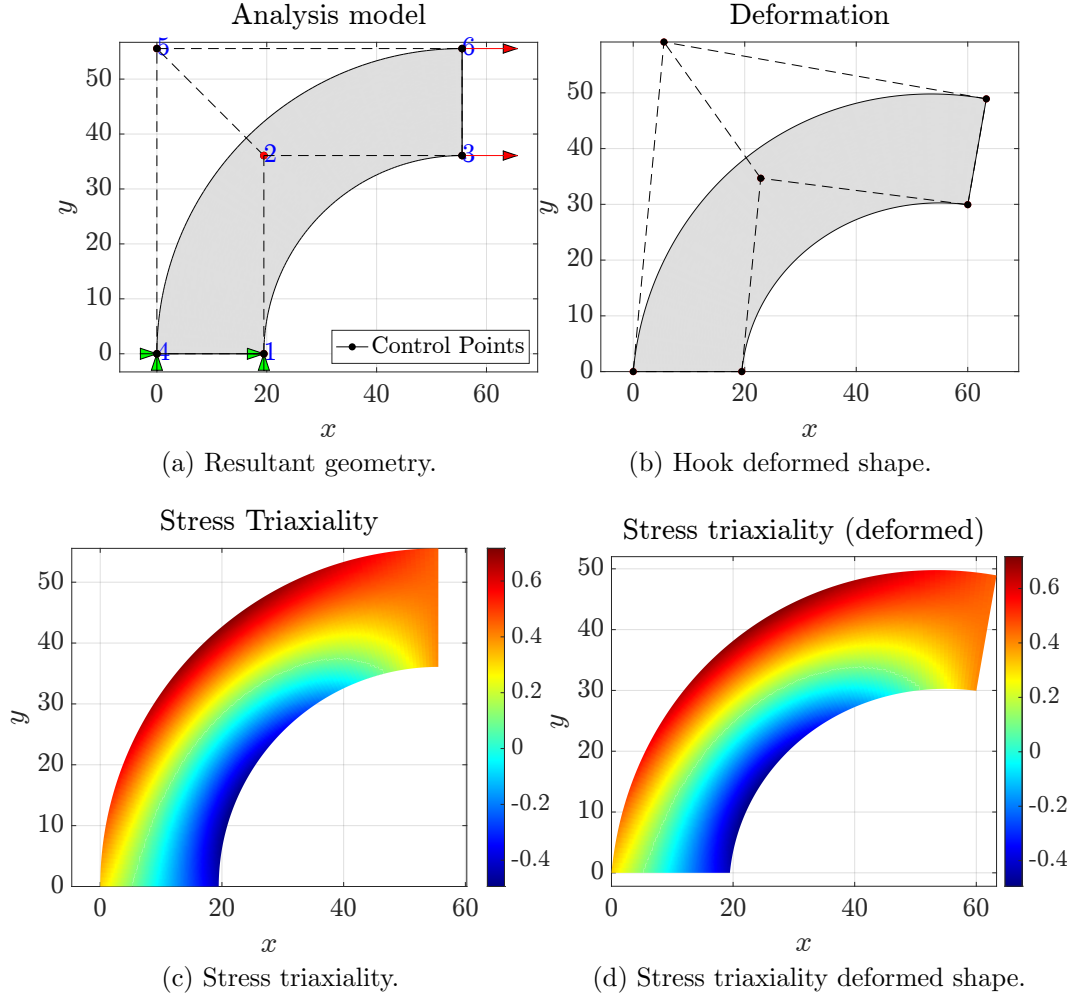


Figure 7: Resultant geometry and stress triaxiality for the upper bound results. Dimensions in mm.

525 6.2. Solid horseshoe

526 The second example illustrates a geometrically complex but single-patch three-dimensional
527 horseshoe problem adapted from [28, 65]. The objective of the study is to estimate the maximum
528 stress triaxiality in the horseshoe shape subjected to equal and opposite in-plane flat-edge unitary
529 displacements (see Figure 8). The base ends of the horseshoe are fixed in the y -direction, while
530 only the outer corners are fixed in the z -direction. In the x -direction, there is a deterministic
531 prescribed unitary displacement $-u_0$ for the left side (non-positive x -coordinates), while there
532 is a deterministic prescribed unitary displacement u_0 for the right side (positive x -coordinates).
533 Furthermore, the displacements in the x -direction are also restricted at the center of the top of the
534 horseshoe. The material properties of the horseshoe system are assumed to be deterministic and
535 equal to $E = 3 \times 10^7$ N/cm² for Young's modulus and $\nu = 0.3$ for Poisson's ratio. The geometry of

536 the horseshoe is constructed by performing a U-sweep on the cross-section of a square of dimensions
 537 $L \times L$, subtracted by a quarter disk of radius R , which defines the inner edge. The outer edge has a
 538 slightly rounded end defined by the value of L . The horseshoe definition includes a straight portion
 539 of height H , and the distance between the origin and the center of the quarter disk is defined by
 540 r (see Figure 8). It is assumed that the values of the parameters that define the geometry L ,
 541 R , r , and H are uncertain due to lack of knowledge at the early design phase. These geometric
 542 quantities are defined by the intervals $L^I = [3.5, 5.5]$, $R^I = [0.5, 1.5]$, $r^I = [0.9142, 1.9142]$, and
 543 $H^I = [7.5, 8.5]$ in cm. Figure 9 shows the IGA model for stress triaxiality analysis in the horseshoe,
 544 where the geometry representation, as in the hook example, is defined by the midpoints of the
 545 interval variables.

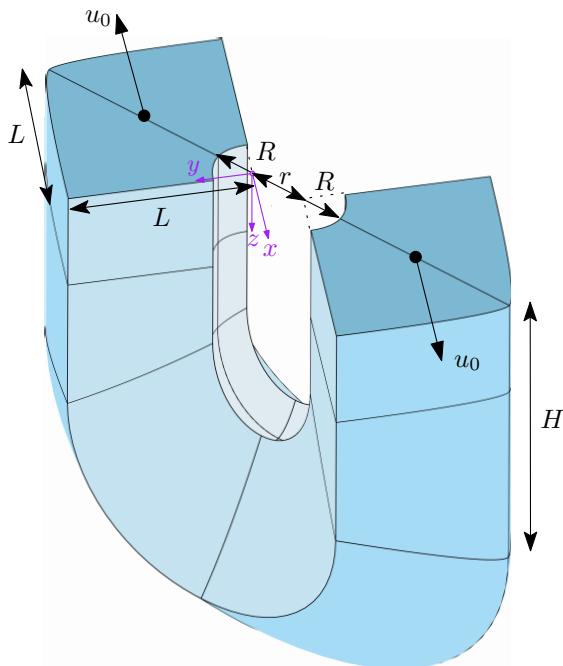


Figure 8: Uncertain geometric parameters of solid horseshoe 3D model for stress triaxiality analysis.

546 The NURBS volume used to represent the horseshoe-shaped geometry is based on $n_{cp} = 108$
 547 control points, which comprises 324 degree-of-freedom. A parametric representation of the coordi-
 548 nates of each control point in terms of L , R , r , and H is proposed to translate the uncertainty in
 549 the geometric input parameters into the NURBS control point matrix. As can be seen in Figure 9,
 550 the control points are strategically placed to achieve the desired curvature and smoothness. To
 551 create the NURBS of the horseshoe, the area of its cross-section was modeled using three curves:
 552 an inner curve (representing the edge created by extracting the quarter disk of radius R), an outer
 553 curve (the opposite side of the extracted quarter disk), and a curve located between the inner and

554 outer curves. Each curve is composed of four control points where, depending on the desired cur-
555 vature, the weights $w_1 = 0.8536$, $w_2 = 0.7071$, $w_3 = 0.6036$, and $w_4 = 1$ were used. These sections
556 were repeated at different heights: $z = 0, \frac{H}{4}, \frac{H}{2}$, for the straight section of the horseshoe, for both
557 ends. Three cross-section areas were used to define the curved portion of the horseshoe. Two of
558 them replicated the cross-section with an inclination of 45 degrees with respect to the plane $z = H$
559 for the left and right side, while the third one was located in the center of the horseshoe geometry
560 with an inclination of 90 degrees with respect to the plane $z = H$. The resulting NURBS volume
561 is composed of displacement-based solid elements. The polynomial degree p of the splines that are
562 associated with the knot vectors is three for the x , y , and z -dimension. The knot vectors used
563 to define the parametric space are:

$$\mathbf{\Xi} = \{0, 0, 0, \frac{1}{2}, 1, 1, 1\}, \mathbf{H} = \{0, 0, 0, 1, 1, 1\}, \mathbf{Z} = \{0, 0, 0, \frac{1}{6}, \frac{2}{6}, \frac{1}{2}, \frac{1}{2}, \frac{4}{6}, \frac{5}{6}, 1, 1, 1\}. \quad (36)$$

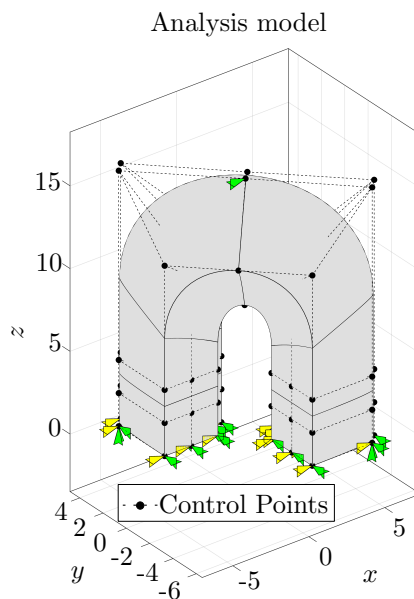


Figure 9: Solid horseshoe 3D model for stress triaxiality analysis. The geometry considered corresponds to that described by the midpoints of the intervals associated with the uncertain parameters. Dimensions in cm.

564 The lower and upper bounds of the maximum stress triaxiality σ_{5T} in the horseshoe system
565 are determined using a gradient-based optimization approach, taking advantage of the sensitiv-
566 ities computed along with the IGA model. The starting point for the optimization scheme was
567 considered as $x_0 = [\mu_{LI}, \mu_{RI}, \mu_{rI}, \mu_{HI}]$. The results were compared by considering the Vertex
568 Method (VM) [52], Particle Swarm Optimization (PSO) [62], Surrogate Optimization (SO) using
569 the Radial Basis Function (RBF) interpolation algorithm available in `Matlab` [63], and Pattern

570 Search Optimization (PS) [64], similar to the first example. Table 3 shows the results for the lower
571 bound of the maximum stress triaxiality of the solid horseshoe. The geometric parameters (R , r ,
572 L , H) are also listed for each method, along with the number of deterministic analyses performed.
573 While VM requires the least number of analyses (16), it underestimates the lower bound of the
574 stress triaxiality, reflecting a non-monotonic behavior of the response of interest with respect to
575 the uncertain parameters. It is important to note that in this example, due to the number of
576 uncertain parameters considered in the analysis, it is not possible to visualize the behavior of
577 the stress triaxiality in the search space as it was possible in the first example. Regarding the
578 results obtained by the applied optimization schemes, PSO, SO, and PS achieve the smaller value
579 for the lower bound; however, PSO requires a significantly higher computational effort of 4797
580 analyses, making it less efficient. Overall, GBO provides the best balance between accuracy and
581 computational complexity, requiring only 26 analyses.

Method	R in cm	r in cm	L in cm	H in cm	$\max(\sigma_{ST})$	No. Analysis
Vertex Method (VM)	0.5000	0.9142	3.5000	8.5000	3.3271	16
Particle Swarm Optimization (PSO)	0.5000	0.9142	4.5328	8.5000	3.3186	4797
Surrogate Optimization (SO)	0.5000	0.9142	4.5327	8.4996	3.3186	200
Pattern Search Optimization (PS)	0.5000	0.9142	4.5328	8.5000	3.3186	212
Gradient-based Optimization (GBO)	0.5017	0.9187	4.5220	8.4973	3.3203	26

Table 3: Results of optimization - lower bound of maximum stress triaxiality - horseshoe 3D.

582 The resulting geometry for the horseshoe system with the optimal values of the uncertain
583 parameters for the lower bound of the response is shown in Figure 10.a. As expected, the lower
584 limit of the maximum stress triaxiality is associated with a thicker section geometry, defined by
585 a high value of L and H , and a smaller value of R and r . Figure 10.b shows the deformed shape
586 due to the equal and opposite in-plane flat-edge unitary displacements. Note how the horseshoe
587 tends to deflect its ends outward.

588 Figure 11 illustrates the stress triaxiality distribution for the geometry corresponding to the
589 lower bound of the response. Specifically, Figures 11.a and 11.b depict the stress triaxiality in the
590 xy -plane, while Figures 11.c and 11.d show the stress triaxiality in the xz -plane. In particular,

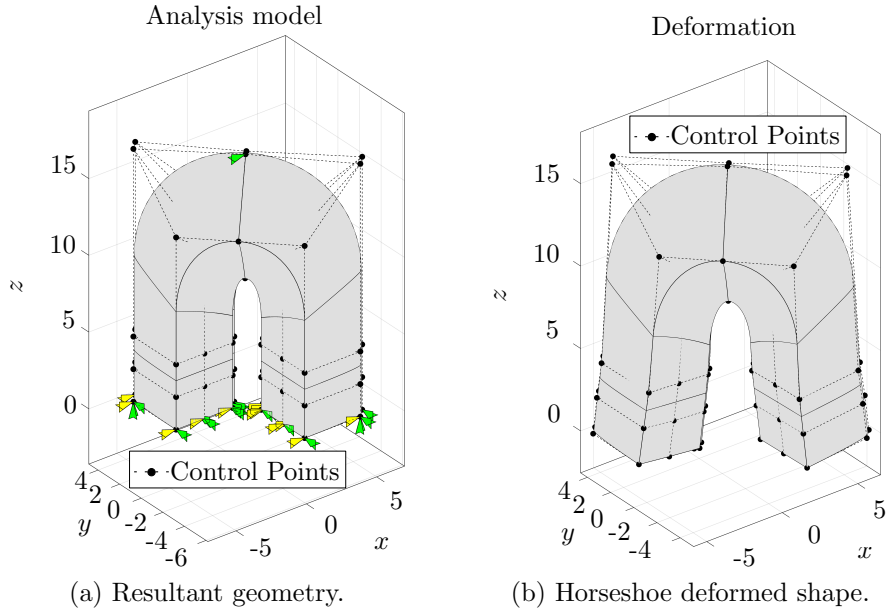
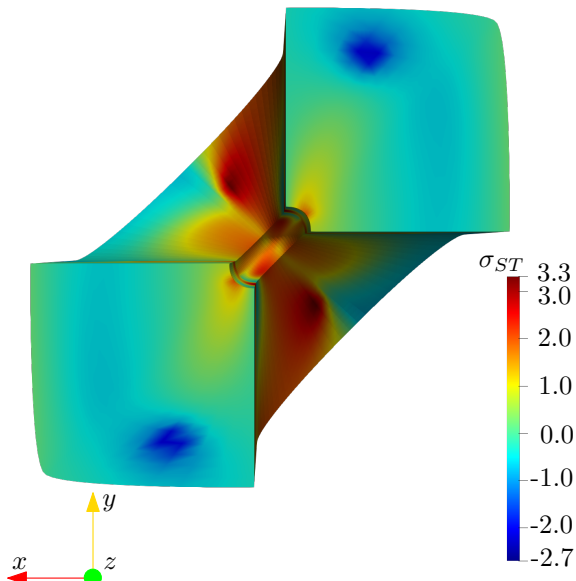


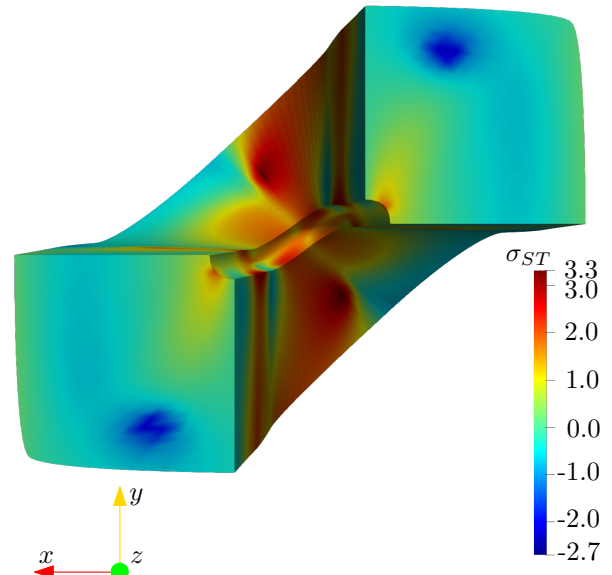
Figure 10: Resultant geometry for the lower bound results for the 3D horseshoe. Dimensions in cm.

591 Figures 11.b and 11.d highlight the stress triaxiality distribution in the deformed configuration.
 592 To understand these triaxial stress results, Figure 12 shows the hydrostatic and von Mises stresses
 593 on the deformed horseshoe in the xy and xz planes. The highest concentration of hydrostatic
 594 stress is observed in the inner upper region of the horseshoe shape (see Figure 12), leading to
 595 an increased stress triaxiality (3.3) in this region (as shown in Figure 11). Zones of significant
 596 deformation coincide with regions of high stress, indicating potential brittle failure since increased
 597 stress triaxiality typically favors brittle fracture over ductile behavior. As shown in Figure 8,
 598 this stress distribution is expected due to the application of opposing in-plane flat-edge unitary
 599 displacements. The calculated stress values, including both hydrostatic and von Mises stresses
 600 (see Figure 12), are consistent with results reported in the literature [28, 65].

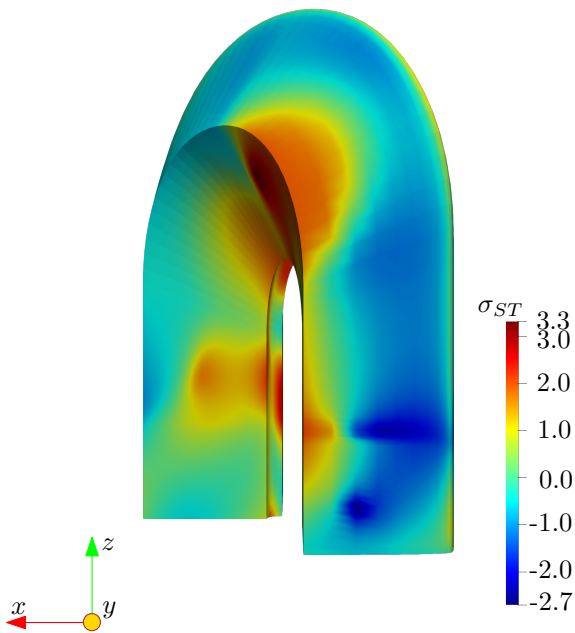
601 The results for the upper bound of the maximum stress triaxiality of the solid horseshoe are
 602 shown in Table 4. The optimal value of the geometric parameters (R, r, L, H) is also shown for
 603 each optimization method used, along with the number of deterministic analyses performed. The
 604 Vertex Method requires the least number of iterations (16). However, it underestimates the upper
 605 bound of the stress triaxiality as well as the case for the lower bound. The same optimum value for
 606 the maximum stress triaxiality is achieved by all optimization algorithms considered. Nevertheless,
 607 PSO requires significantly more computations (4665), making it less efficient, than for example,
 608 SO and PS. The Gradient-based Optimization method, which requires only 20 analyses, offers the



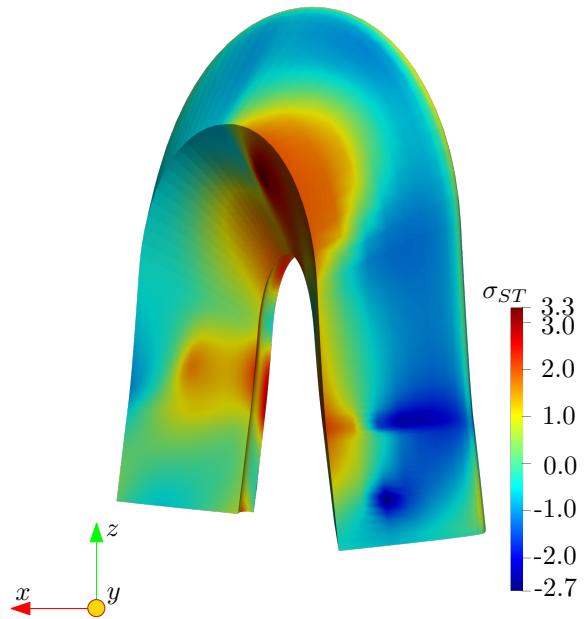
(a) Stress triaxiality (in-plane view).



(b) Stress triaxiality deformed shape (in-plane view).



(c) Stress triaxiality.



(d) Stress triaxiality deformed shape.

Figure 11: Stress triaxiality for the lower bound results for the 3D horseshoe.

609 best trade-off between accuracy and computational complexity, showing the benefit of using the
 610 sensitivities from the variational approach.

611 Similar to the lower bound, Figure 13.a shows the resulting geometry for the horseshoe system
 612 with the optimal values of the uncertain geometric parameters for the upper bound of the response.

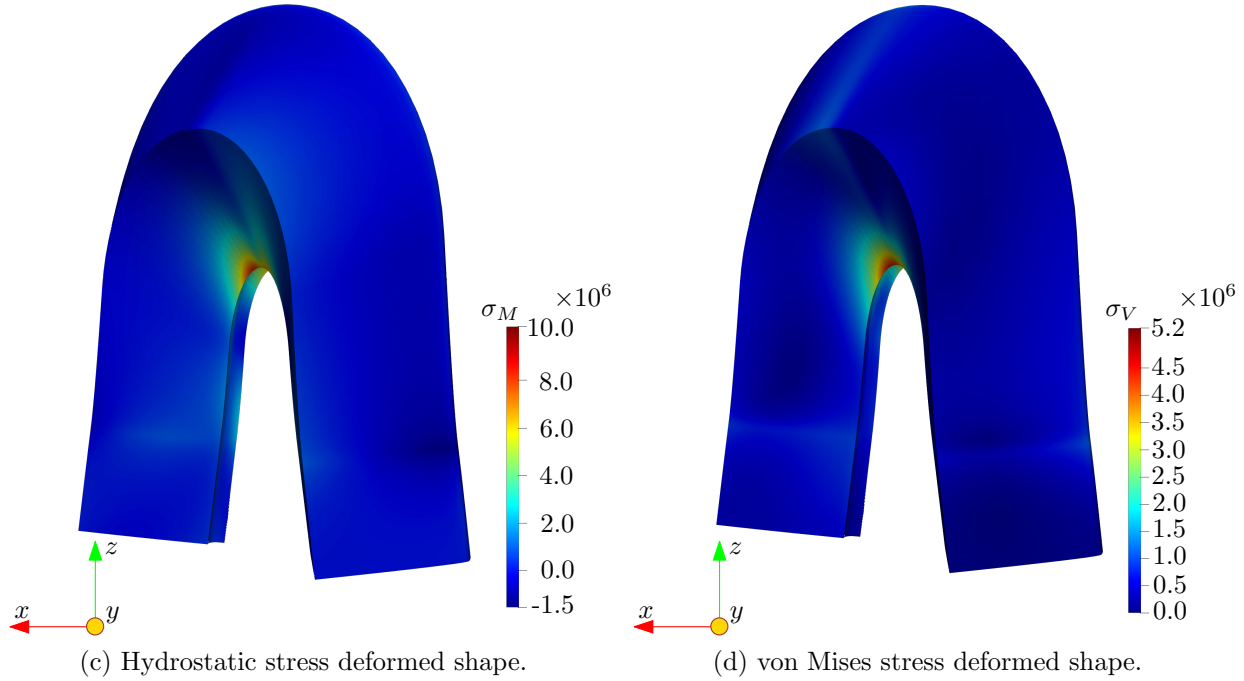
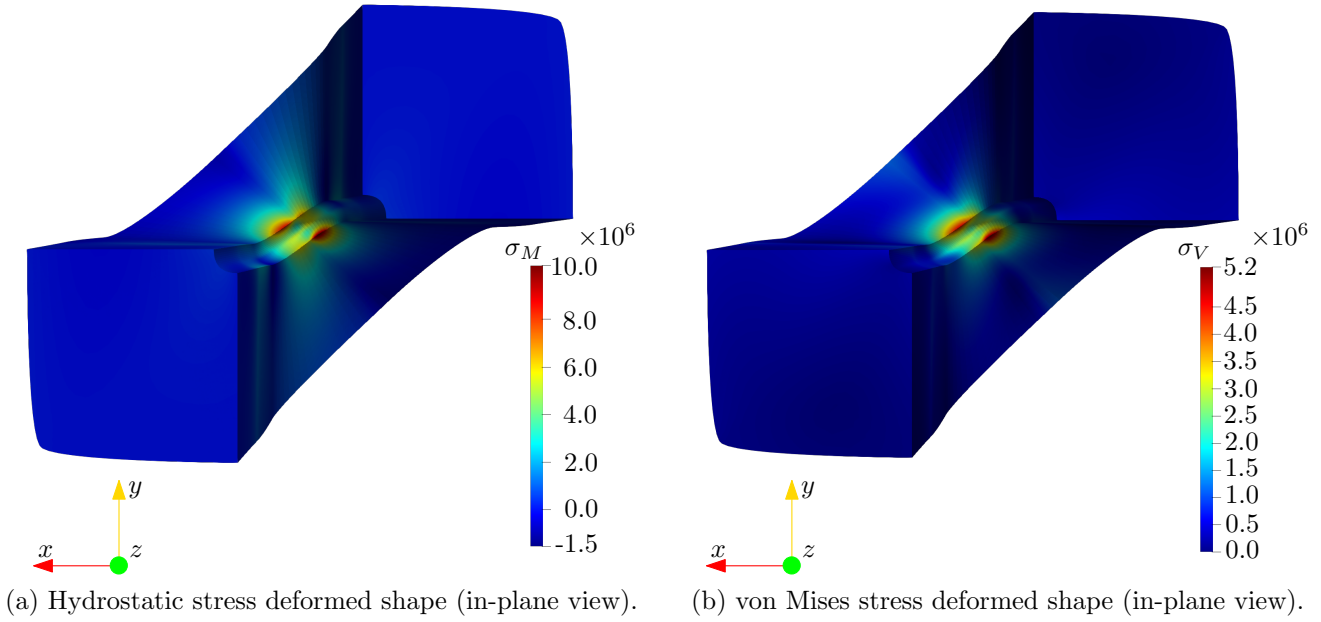


Figure 12: Stresses for the lower bound results for the 3D horseshoe, in consistent units in Example 2.

613 As expected, the upper bound of the maximum stress triaxiality is associated with a thin section
 614 geometry defined by a low value of L and H , a higher value of R , and more separation between
 615 the two ends of the horseshoe, i.e., a high value of r . Figure 13.b shows the deformed shape due
 616 to the equal and opposite in-plane flat-edge unitary displacements.

Method	R in cm	r in cm	L in cm	H in cm	$\max(\sigma_{ST})$	No. Analysis
Vertex Method (VM)	1.5000	0.9142	3.5000	8.5000	4.9551	16
Particle Swarm Optimization (PSO)	1.5000	1.7979	3.6653	7.5000	5.0209	4665
Surrogate Optimization (SO)	1.5000	1.7991	3.6662	7.5000	5.0209	200
Pattern Search Optimization (PS)	1.5000	1.7979	3.6652	7.5000	5.0209	651
Gradient-based Optimization (GBO)	1.5000	1.7978	3.6652	7.5000	5.0209	20

Table 4: Results of optimization - upper bound of maximum stress triaxiality - horseshoe 3D.

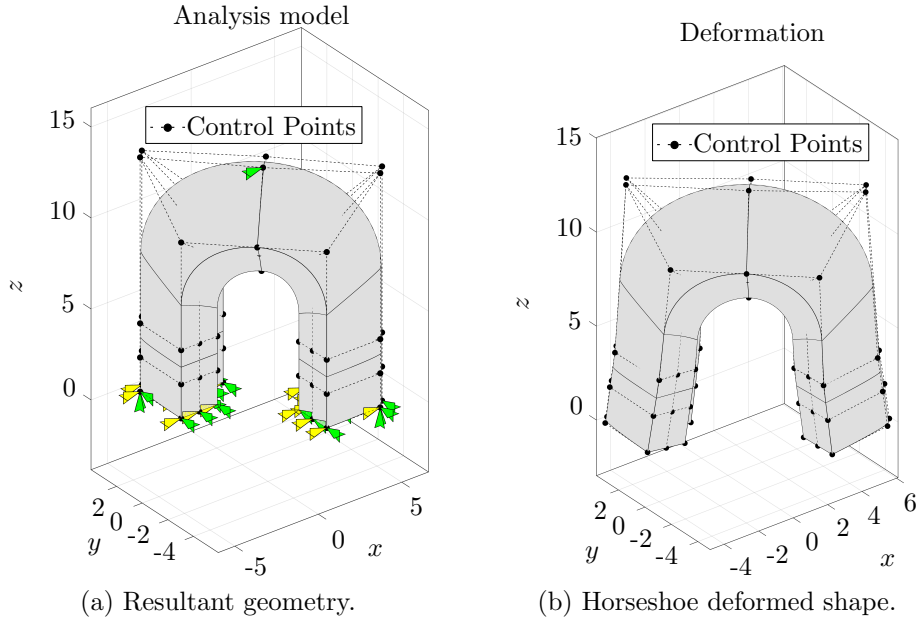


Figure 13: Resultant geometry for the upper bound results for the 3D horseshoe. Dimensions in cm.

617 On the other hand, Figure 14 shows the stress triaxiality distribution within the horseshoe
618 shape resulting from the imposed unitary displacements for the geometry resulting from the up-
619 per bound. Comparing these results with those from the lower bound geometry (see Figure 11)
620 shows how geometric changes affect the stress distribution. Nevertheless, the regions of high-stress
621 concentration remain consistent in the same areas of the horseshoe. For the upper bound geom-
622 etry, the stress triaxiality has a more homogeneous pattern, but with a wider range of values.
623 In addition, the regions of high-stress triaxiality (5) are more concentrated compared to those
624 observed in the lower-bound scenario. The elevated stress triaxiality values shown in Figure 14

625 indicate critical areas that are susceptible to failure. As before, these critical areas are located
626 where significant deformation occurs. To gain a comprehensive understanding of the stress tri-
627 axiality distribution, Figure 15 illustrates the hydrostatic and von Mises stresses in the deformed
628 shape. A significant concentration of both stress types is observed in the inner portion of the
629 horseshoe, with the highest values occurring in the upper inner area.

630 In optimization procedures involving geometric parameters, ensuring the regularity of the
631 stiffness matrix is essential to guarantee numerical stability and physical validity. In the examples
632 studied, the determinant of the local deformation gradient was consistently positive, indicating
633 the presence of physically valid configurations without element inversion. As anticipated for linear
634 elasticity with suitable boundary conditions, the stiffness matrix remained nonsingular in these
635 cases. Nevertheless, a significant deviation of the control points from their nominal positions could
636 result in a negative determinant, leading to unphysical behavior, as this implies a negative mass
637 density. Consequently, additional measures could be incorporated into the optimization process
638 to overcome this potential problem. For example, constraints could be applied to maintain a
639 minimum distance between certain control points to avoid self-penetration of the mesh. While
640 these precautions are not necessary in the examples studied, they could prove valuable for complex
641 geometries or extreme deformations.

642 **7. Summary and conclusions**

643 This paper explores the application of isogeometric analysis (IGA) with interval analysis for
644 efficient quantification of the effects of geometric uncertainties on the performance of mechanical
645 systems. The study focused on estimating the bounds of maximum stress triaxiality in a 2D hook
646 system with uncertain radius and thickness parameters, and a solid 3D horseshoe shape with four
647 uncertain geometric parameters.

648 According to the results, the implemented method, which utilizes the gradient-based optimiza-
649 tion (GBO) approach to estimate the bounds of the response, significantly reduces the compu-
650 tational cost associated with uncertainty quantification in an interval context. The efficiency of
651 the method is due to the ability of the IGA model to directly manipulate geometry and compute
652 sensitivities without the need for costly remeshing. This benefit is achieved due to the application
653 of a variational sensitivity analysis that allows one to compute the change of the response function
654 concerning alterations in the uncertain parameters along with the calculation of the response of

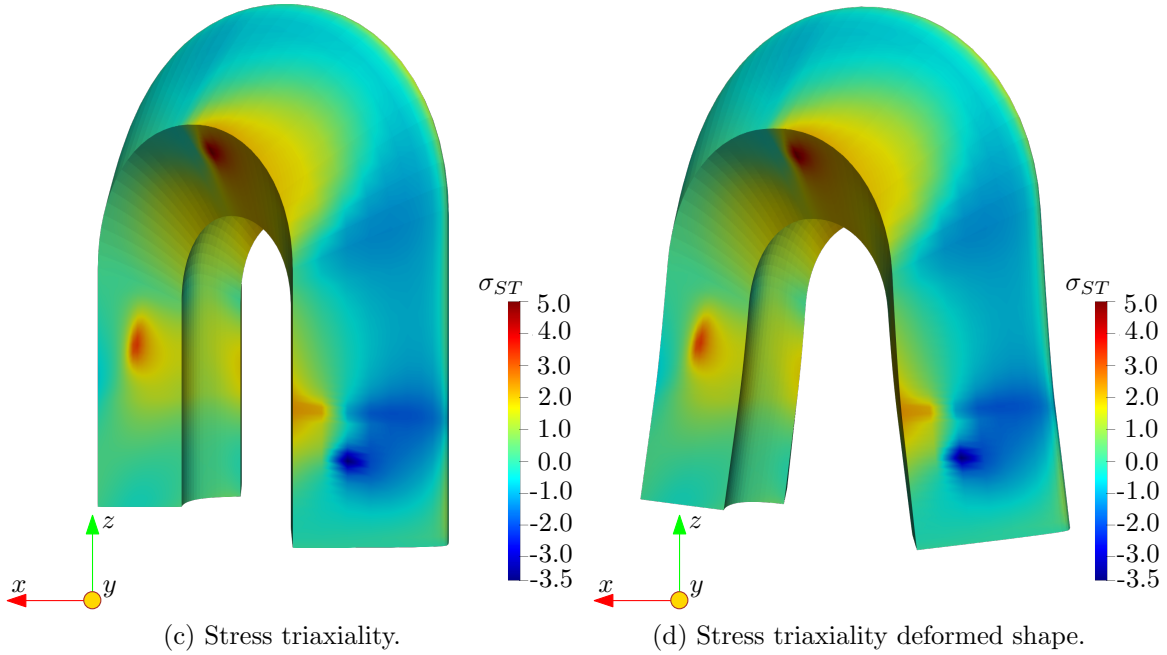
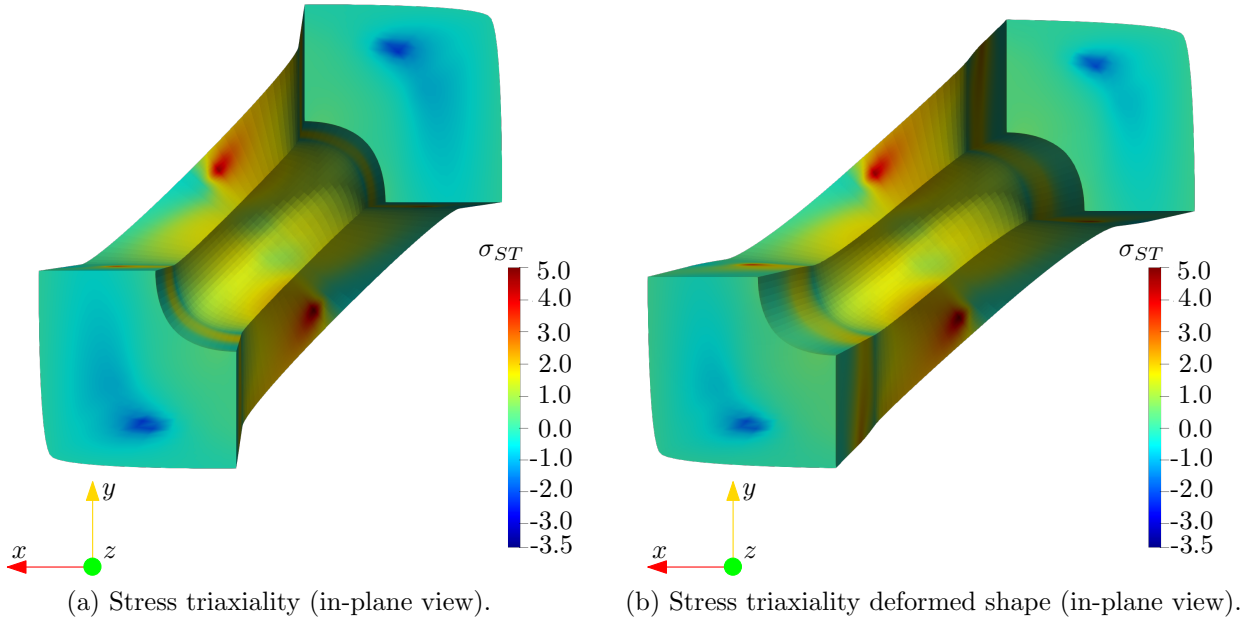
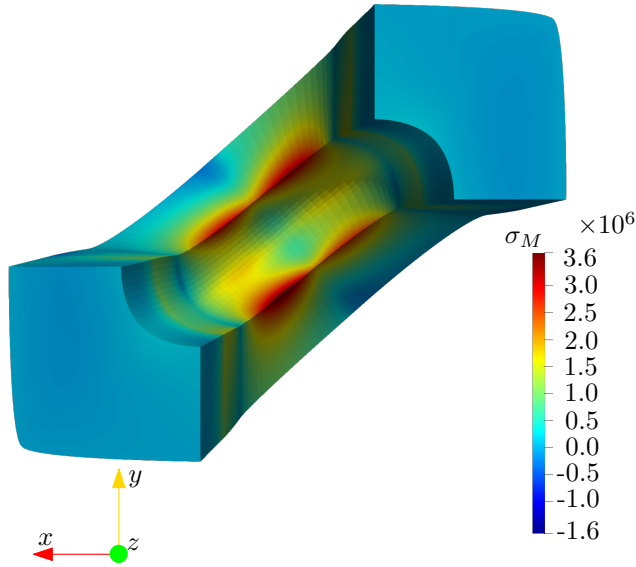
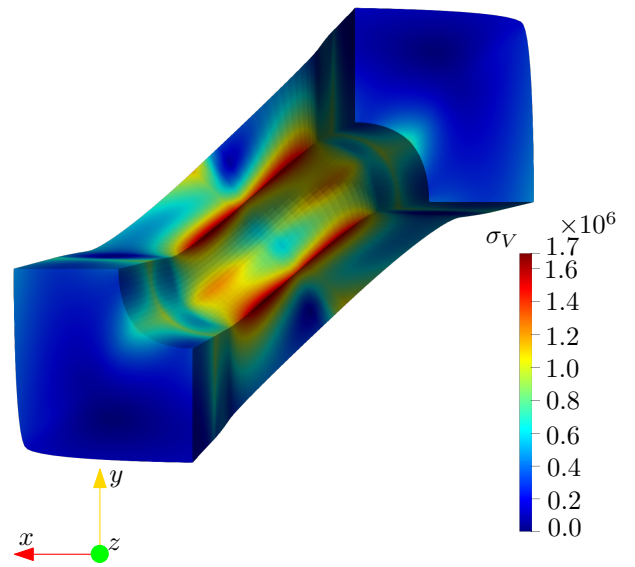


Figure 14: Stress triaxiality for the upper bound results for the 3D horseshoe.

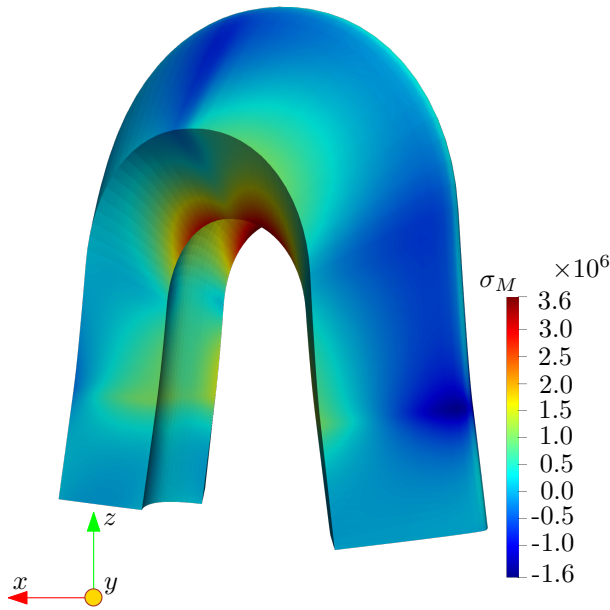
655 interest. To enhance the potential of IGA for uncertainty quantification within finite element
 656 users, a parametric description of the control point matrix is proposed. This approach allows
 657 the direct translation of geometric uncertainties into the NURBS used for system representation.
 658 By incorporating uncertainty directly into the NURBS framework, this method facilitates the
 659 integration of IGA into traditional FEA workflows for geometric variation in mechanical systems.



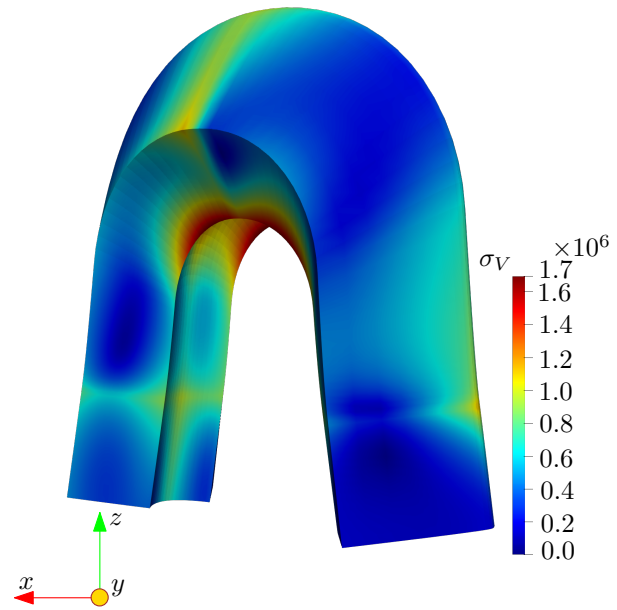
(a) Hydrostatic stress deformed shape (in-plane view).



(b) von Mises stress deformed shape (in-plane view).



(c) Hydrostatic stress deformed shape.



(d) von Mises stress deformed shape.

Figure 15: Stresses for the lower bound results for the 3D horseshoe, in consistent units in Example 2.

660 Future work will explore the application of this method to more complex systems requiring
 661 multiple patches for their construction, and investigate its potential for other types of uncertainty
 662 description techniques, such as interval fields. In this case, the advantages of describing and
 663 propagating uncertainty using NURBS-based interval fields will be investigated. Moreover, while
 664 the present study is concerned with cases involving a limited number of uncertain parameters,

665 extending the framework to encompass high-dimensional uncertainties, such as surface geometric
666 uncertainties would be a logical subsequent step. Since interval fields reduce the uncertainty to
667 that contained at the control point positions, the key to dealing with high-dimensional geometric
668 uncertainty will be to strategically determine which NURBS control points should be treated as
669 uncertain and which should be used solely to manipulate the geometry. Therefore, the methodol-
670 ogy will be further examined for coupling with mesh refinement in IGA for complex geometries.

671 Acknowledgement

672 Financial support by the Deutsche Forschungsgemeinschaft (DFG, German Research Founda-
673 tion) – Project-ID 278868966 – TRR188 is gratefully acknowledged.

674 References

- 675 [1] J. Kim, I. Lee, Modeling of geometric uncertainties in topology optimization via the shift
676 of design nodes, *Structural and Multidisciplinary Optimization* 65 (7) (Jun. 2022). doi:
677 10.1007/s00158-022-03277-y.
- 678 [2] J. Wang, B. Wang, H. Yang, Z. Sun, K. Zhou, X. Zheng, Compressor geometric uncertainty
679 quantification under conditions from near choke to near stall, *Chinese Journal of Aeronautics*
680 36 (3) (2023) 16–29. doi:10.1016/j.cja.2022.10.012.
- 681 [3] W. Chu, T. Ji, X. Chen, B. Luo, Mechanism analysis and uncertainty quantification of
682 blade thickness deviation on rotor performance, *Proceedings of the Institution of Me-
683 chanical Engineers, Part A: Journal of Power and Energy* (2023) 095765092311621doi:
684 10.1177/09576509231162143.
- 685 [4] H. Zhang, J. Guillemot, L. J. Gomez, Stochastic modeling of geometrical uncertainties on
686 complex domains, with application to additive manufacturing and brain interface geometries,
687 *Computer Methods in Applied Mechanics and Engineering* 385 (2021) 114014. doi:10.1016/
688 j.cma.2021.114014.
- 689 [5] H. Cheng, Z. Li, P. Duan, X. Lu, S. Zhao, Y. Zhang, Robust optimization and uncertainty
690 quantification of a micro axial compressor for unmanned aerial vehicles, *Applied Energy* 352
691 (2023) 121972. doi:10.1016/j.apenergy.2023.121972.

- 692 [6] G. Kim, S. M. Yang, D. M. Kim, S. Kim, J. G. Choi, M. Ku, S. Lim, H. W. Park, Bayesian-
693 based uncertainty-aware tool-wear prediction model in end-milling process of titanium alloy,
694 Applied Soft Computing 148 (2023) 110922. doi:10.1016/j.asoc.2023.110922.
- 695 [7] T. Cheng, S. Xiang, H. Zhang, J. Yang, New machining test for identifying geometric and
696 thermal errors of rotary axes for five-axis machine tools, Measurement 223 (2023) 113748.
697 doi:10.1016/j.measurement.2023.113748.
- 698 [8] Y. Altintas, A. Verl, C. Brecher, L. Uriarte, G. Pritschow, Machine tool feed drives, CIRP
699 Annals 60 (2) (2011) 779–796. doi:10.1016/j.cirp.2011.05.010.
- 700 [9] J. Liu, A. T. Gaynor, S. Chen, Z. Kang, K. Suresh, A. Takezawa, L. Li, J. Kato, J. Tang,
701 C. C. L. Wang, L. Cheng, X. Liang, A. C. To, Current and future trends in topology opti-
702 mization for additive manufacturing, Structural and Multidisciplinary Optimization 57 (6)
703 (2018) 2457–2483. doi:10.1007/s00158-018-1994-3.
- 704 [10] N. Nie, L. Su, G. Deng, H. Li, H. Yu, A. K. Tieu, A review on plastic deformation induced
705 surface/interface roughening of sheet metallic materials, Journal of Materials Research and
706 Technology 15 (2021) 6574–6607. doi:10.1016/j.jmrt.2021.11.087.
- 707 [11] X. Zhang, W. Yang, M. Li, An Uncertainty Approach for Fixture Layout Optimization
708 Using Monte Carlo Method, Springer Berlin Heidelberg, 2010, pp. 10–21. doi:10.1007/
709 978-3-642-16587-0_2.
- 710 [12] F. N. Schietzold, A. Schmidt, M. M. Dannert, A. Fau, R. M. N. Fleury, W. Graf, M. Kaliske,
711 C. Könke, T. Lahmer, U. Nackenhorst, Development of fuzzy probability based random
712 fields for the numerical structural design, GAMM-Mitteilungen 42 (1) (2019) e201900004.
713 doi:10.1002/gamm.201900004.
- 714 [13] M. Faes, M. Broggi, E. Patelli, Y. Govers, J. Mottershead, M. Beer, D. Moens, A multivariate
715 interval approach for inverse uncertainty quantification with limited experimental data, Me-
716 chanical Systems and Signal Processing 118 (2019) 534–548. doi:10.1016/j.ymsp.2018.
717 08.050.
- 718 [14] B. Möller, M. Beer, Fuzzy Randomness, Springer Berlin Heidelberg, 2004. doi:10.1007/
719 978-3-662-07358-2.

- 720 [15] D. Zhang, L. Shu, S. Li, Fuzzy structural element method for solving fuzzy dual medium
721 seepage model in reservoir, *Soft Computing* 24 (21) (2020) 16097–16110. doi:10.1007/
722 s00500-020-04926-4.
- 723 [16] M. G. Faes, M. Daub, S. Marelli, E. Patelli, M. Beer, Engineering analysis with probability
724 boxes: A review on computational methods, *Structural Safety* 93 (2021) 102092. doi:10.
725 1016/j.strusafe.2021.102092.
- 726 [17] M. G. Faes, M. Broggi, G. Chen, K.-K. Phoon, M. Beer, Distribution-free p-box processes
727 based on translation theory: Definition and simulation, *Probabilistic Engineering Mechanics*
728 69 (2022) 103287. doi:10.1016/j.probengmech.2022.103287.
- 729 [18] D. Degrauwe, G. Lombaert, G. D. Roeck, Improving interval analysis in finite element cal-
730 culations by means of affine arithmetic, *Computers & Structures* 88 (3-4) (2010) 247–254.
731 doi:10.1016/j.compstruc.2009.11.003.
- 732 [19] A. Sofi, E. Romeo, A novel Interval Finite Element Method based on the improved interval
733 analysis, *Computer Methods in Applied Mechanics and Engineering* 311 (2016) 671–697.
734 doi:http://dx.doi.org/10.1016/j.cma.2016.09.009.
735 URL <http://www.sciencedirect.com/science/article/pii/S004578251631129X>
- 736 [20] R. R. Callens, M. G. Faes, D. Moens, Multilevel Quasi-Monte Carlo for Interval Analysis,
737 *International Journal for Uncertainty Quantification* 12 (4) (2022) 1–19. doi:10.1615/int.
738 j.uncertaintyquantification.2022039245.
- 739 [21] C. Dang, P. Wei, M. G. Faes, M. A. Valdebenito, M. Beer, Interval uncertainty propagation by
740 a parallel bayesian global optimization method, *Applied Mathematical Modelling* 108 (2022)
741 220–235. doi:10.1016/j.apm.2022.03.031.
- 742 [22] V. Kreinovich, A. Lakeyev, J. Rohn, P. Kahl, *Computational Complexity and Feasibil-*
743 *ity of Data Processing and Interval Computations*, Springer US, 1998. doi:10.1007/
744 978-1-4757-2793-7.
- 745 [23] M. Beer, Y. Zhang, S. T. Quek, K. K. Phoon, Reliability analysis with scarce information:
746 Comparing alternative approaches in a geotechnical engineering context, *Structural Safety* 41
747 (2013) 1–10. doi:10.1016/j.strusafe.2012.10.003.

- 748 [24] R. E. Moore, *Methods and Applications of Interval Analysis*, Society for Industrial and Ap-
749 plied Mathematics, 1979. doi:10.1137/1.9781611970906.
- 750 [25] A. Sofi, E. Romeo, O. Barrera, A. Cocks, An interval finite element method for the analysis of
751 structures with spatially varying uncertainties, *Advances in Engineering Software* 128 (2019)
752 1–19. doi:10.1016/j.advengsoft.2018.11.001.
- 753 [26] M. Faes, D. Moens, Recent trends in the modeling and quantification of non-probabilistic
754 uncertainty, *Archives of Computational Methods in Engineering* 27 (3) (2019) 633–671. doi:
755 10.1007/s11831-019-09327-x.
- 756 [27] D. Moens, D. Vandepitte, Interval sensitivity theory and its application to frequency response
757 envelope analysis of uncertain structures, *Computer Methods in Applied Mechanics and En-*
758 *gineering* 196 (21) (2007) 2486–2496. doi:<https://doi.org/10.1016/j.cma.2007.01.006>.
759 URL <https://www.sciencedirect.com/science/article/pii/S0045782507000187>
- 760 [28] T. Hughes, J. Cottrell, Y. Bazilevs, Isogeometric analysis: Cad, finite elements, nurbs, exact
761 geometry and mesh refinement, *Computer Methods in Applied Mechanics and Engineering*
762 194 (39–41) (2005) 4135–4195. doi:10.1016/j.cma.2004.10.008.
- 763 [29] J. A. Cottrell, *Isogeometric analysis*, Wiley, Chichester, West Sussex, U.K, 2009.
- 764 [30] V. Agrawal, S. S. Gautam, Iga: A simplified introduction and implementation details for
765 finite element users, *Journal of The Institution of Engineers (India): Series C* 100 (3) (2018)
766 561–585. doi:10.1007/s40032-018-0462-6.
- 767 [31] W. Wang, G. Chen, D. Yang, Z. Kang, Stochastic isogeometric analysis method for plate
768 structures with random uncertainty, *Computer Aided Geometric Design* 74 (2019) 101772.
769 doi:10.1016/j.cagd.2019.101772.
- 770 [32] E. Wobbes, Y. Bazilevs, T. Kuraishi, Y. Otaguro, K. Takizawa, T. E. Tezduyar, Complex-
771 geometry iga mesh generation: application to structural vibrations, *Computational Mechanics*
772 74 (2) (2024) 247–261. doi:10.1007/s00466-023-02432-6.
- 773 [33] T. D. Hien, H.-C. Noh, Stochastic isogeometric analysis of free vibration of functionally
774 graded plates considering material randomness, *Computer Methods in Applied Mechanics*
775 *and Engineering* 318 (2017) 845–863. doi:10.1016/j.cma.2017.02.007.

- 776 [34] K. Li, W. Gao, D. Wu, C. Song, T. Chen, Spectral stochastic isogeometric analysis of linear
777 elasticity, *Computer Methods in Applied Mechanics and Engineering* 332 (2018) 157–190.
778 doi:10.1016/j.cma.2017.12.012.
- 779 [35] P. Hao, H. Tang, Y. Wang, T. Wu, S. Feng, B. Wang, Stochastic isogeometric buckling anal-
780 ysis of composite shell considering multiple uncertainties, *Reliability Engineering & System
781 Safety* 230 (2023) 108912. doi:10.1016/j.ress.2022.108912.
- 782 [36] X. Lin, W. Zheng, F. Zhang, H. Chen, Uncertainty quantification and robust shape optimiza-
783 tion of acoustic structures based on iga bem and polynomial chaos expansion, *Engineering
784 Analysis with Boundary Elements* 165 (2024) 105770. doi:10.1016/j.enganabound.2024.
785 105770.
- 786 [37] H. Zhang, T. Shibusaki, Development of stochastic isogeometric analysis (siga) method for
787 uncertainty in shape, *International Journal for Numerical Methods in Engineering* 118 (1)
788 (2018) 18–37. doi:10.1002/nme.6008.
- 789 [38] X. Zhang, J. Gao, L. Gao, M. Xiao, B-ito: A matlab toolbox for isogeometric topology
790 optimization with bézier extraction of nurbs, *Advances in Engineering Software* 191 (2024)
791 103620. doi:10.1016/j.advengsoft.2024.103620.
- 792 [39] V. P. Nguyen, C. Anitescu, S. P. Bordas, T. Rabczuk, Isogeometric analysis: An overview
793 and computer implementation aspects, *Mathematics and Computers in Simulation* 117 (2015)
794 89–116. doi:10.1016/j.matcom.2015.05.008.
- 795 [40] N. Antonelli, R. Aristio, A. Gorgi, R. Zorrilla, R. Rossi, G. Scovazzi, R. Wüchner, The
796 shifted boundary method in isogeometric analysis, *Computer Methods in Applied Mechanics
797 and Engineering* 430 (2024) 117228. doi:10.1016/j.cma.2024.117228.
- 798 [41] J. A. Snyman, D. N. Wilke, *Practical Mathematical Optimization*, Springer International
799 Publishing, 2018. doi:10.1007/978-3-319-77586-9.
- 800 [42] J. Liedmann, F.-J. Barthold, Variational sensitivity analysis of elastoplastic structures applied
801 to optimal shape of specimens, *Structural and Multidisciplinary Optimization* 61 (6) (2020)
802 2237–2251. doi:10.1007/s00158-020-02492-9.
- 803 [43] O. C. Zienkiewicz, *The finite element method*, Butterworth-Heinemann, 2000.

- 804 [44] K. W. Morton, D. F. Mayers, Numerical solution of partial differential equations: an intro-
805 duction, Cambridge university press, 2005.
- 806 [45] K.-J. Bathe, Finite Element Procedures, Klaus-Jürgen Bathe, 2014.
- 807 [46] A. Tekkaya, P.-O. Bouchard, S. Bruschi, C. Tasan, Damage in metal forming, CIRP Annals
808 69 (2) (2020) 600–623. doi:10.1016/j.cirp.2020.05.005.
- 809 [47] M. Böddecker, M. Faes, A. Menzel, M. Valdebenito, Effect of uncertainty of material param-
810 eters on stress triaxiality and lode angle in finite elasto-plasticity—a variance-based global
811 sensitivity analysis, Advances in Industrial and Manufacturing Engineering 7 (2023) 100128.
812 doi:10.1016/j.aime.2023.100128.
- 813 [48] Y. Bao, T. Wierzbicki, On fracture locus in the equivalent strain and stress triaxiality space,
814 International Journal of Mechanical Sciences 46 (1) (2004) 81–98. doi:10.1016/j.ijmecsci.
815 2004.02.006.
- 816 [49] D. Moens, M. Hanss, Non-probabilistic finite element analysis for parametric uncertainty
817 treatment in applied mechanics: Recent advances, Finite Elements in Analysis and Design
818 47 (1) (2011) 4–16. doi:10.1016/j.finel.2010.07.010.
- 819 [50] T. Haag, J. Herrmann, M. Hanss, Identification procedure for epistemic uncertainties using
820 inverse fuzzy arithmetic, Mechanical Systems and Signal Processing 24 (7) (2010) 2021–2034.
821 doi:10.1016/j.ymsp.2010.05.010.
- 822 [51] M. Hanss, S. Turrin, A fuzzy-based approach to comprehensive modeling and analysis of
823 systems with epistemic uncertainties, Structural Safety 32 (6) (2010) 433–441. doi:10.
824 1016/j.strusafe.2010.06.003.
- 825 [52] W. Dong, H. C. Shah, Vertex method for computing functions of fuzzy variables, Fuzzy Sets
826 and Systems 24 (1) (1987) 65–78. doi:10.1016/0165-0114(87)90114-x.
- 827 [53] S. S. Rao, L. Berke, Analysis of uncertain structural systems using interval analysis, AIAA
828 Journal 35 (4) (1997) 727–735. doi:10.2514/2.164.
- 829 [54] L. Catallo, Genetic anti-optimization for reliability structural assessment of precast con-
830 crete structures, Computers & Structures 82 (13–14) (2004) 1053–1065. doi:10.1016/j.
831 compstruc.2004.03.018.

- 832 [55] A. Klimke, R. Nunes, B. Wohlmuth, Fuzzy arithmetic based on dimension-adaptive sparse
833 grids: A case study of a large-scale finite element model under uncertain parameters, In-
834 ternational Journal of Uncertainty, Fuzziness and Knowledge-Based Systems 14 (05) (2006)
835 561–577. doi:10.1142/s0218488506004199.
- 836 [56] Z. Deng, Z. Guo, X. Zhang, Interval model updating using perturbation method and radial
837 basis function neural networks, Mechanical Systems and Signal Processing 84 (2017) 699–716.
838 doi:10.1016/j.ymssp.2016.09.001.
- 839 [57] F.-J. Barthold, N. Gerzen, W. Kijanski, D. Materna, Efficient Variational Design Sensitivity
840 Analysis, Vol. 40 of Computational Methods in Applied Sciences, Springer International
841 Publishing, Switzerland, 2016. doi:10.1007/978-3-319-23564-6_14.
- 842 [58] F.-J. Barthold, A short guide to variational design sensitivity analysis, in: 6th World Congress
843 on Structural and Multidisciplinary Optimization, 2005.
- 844 [59] Penguian, Nurbs toolbox by d.m. spnik, MATLAB Central File Exchange Retrieved Decem-
845 ber 14, 2020 (2020).
846 URL [https://www.mathworks.com/matlabcentral/fileexchange/
847 26390-nurbs-toolbox-by-d-m-spink](https://www.mathworks.com/matlabcentral/fileexchange/26390-nurbs-toolbox-by-d-m-spink)
- 848 [60] J. J. Moré, D. C. Sorensen, Computing a trust region step, SIAM Journal on Scientific and
849 Statistical Computing 4 (3) (1983) 553–572. doi:10.1137/0904038.
- 850 [61] R. H. Byrd, J. C. Gilbert, J. Nocedal, A trust region method based on interior point techniques
851 for nonlinear programming, Mathematical Programming 89 (1) (2000) 149–185. doi:10.
852 1007/p100011391.
- 853 [62] J. Kennedy, R. Eberhart, Particle swarm optimization, in: Proceedings of ICNN'95-
854 International Conference on Neural Networks, Vol. 4, IEEE, Perth, WA, Australia, 1995,
855 pp. 1942–1948.
- 856 [63] M. J. D. Powell, The Theory of Radial Basis Function Approximation in 1990, Oxford Uni-
857 versity PressOxford, 1992, pp. 105–210. doi:10.1093/oso/9780198534396.003.0003.
- 858 [64] C. Audet, J. E. Dennis, Analysis of generalized pattern searches, SIAM Journal on Optimiza-
859 tion 13 (3) (2002) 889–903. doi:10.1137/s1052623400378742.

860 [65] R. Jahanbin, S. Rahman, Stochastic isogeometric analysis in linear elasticity, Computer Meth-
861 ods in Applied Mechanics and Engineering 364 (2020) 112928. doi:10.1016/j.cma.2020.
862 112928.